and Use of Laboratory Animals as stated by the National Institutes of Health.

2.5.2. Tumor implantation

BxPC3 cell line (ATCC, Manassas, VA), derived from human pancreatic tumor was inoculated to nude mice subcutaneously to develop xenografts (100 μl of 5×10^7 cells/mL PBS suspension). Tumors were allowed to grow for 3 weeks till their size reached approximately 120–160 mm^3.

2.5.3. Blood circulation

Polyplex micelles loading Cy5-labeled pDNA (100 μg pDNA/mL, 200 μL) were intravenously injected to the mice via the tail vein at a dose of 20 μg pDNA/mouse. Blood was collected from the postcaval vein under anesthesia 15 min after injection and centrifuged to obtain blood plasma. Two microliters of 10X trypsin-EDTA were added to 20 μL of the plasma and incubated overnight at 37 °C to release pDNA from the micelle by digesting PLys segment of the block copolymer. The fluorescence intensity of the sample solution was measured at $\lambda = 670$ nm by spectrofluorometer (ND-3300, Nano Drop, Wilmington, DE), and percent of pDNA dosage in the blood was calculated according to the following equation:

$$\%\ \text{injected pDNA in the blood} = (F_{670(\text{sample})} / F_{670(\text{control})}) \times 100 \quad (1)$$

where the $F_{670(\text{control})}$ represents the fluorescence intensity of micelle solution mixed with blood sample (time 0).

2.5.4. In vivo tumor growth inhibition

Polyplex micelles, loading pDNA equivalent to 20 μg and dissolved in 10 mM Hepes buffer (pH 7.4) with 150 mM NaCl, were administered intravenously on days 0, 4, and 8. Tumor size was measured every 2 days by a digital vernier caliper across its longest (a) and shortest diameters (b) and its volume (V) was calculated according to the formula $V = 0.5ab^2$. Tumor progression was evaluated in terms of relative tumor volume (to day 0) over a period of 18 days.

2.5.5. Quantification of microvessel density

At the end of *in vivo* tumor growth studies, xenografted tumors were excised and frozen in tissue-Tek-OCT. The frozen tumors were cut into 10 μm thick slices with a cryostat maintained at −23 °C. Vascular endothelial cells were immunostained by incubation of the cryosections with anti-CD31 antibody followed by incubation with Alexa Fluor 488-conjugated secondary antibody. The tumor cryosections were observed by a confocal laser scanning microscope (CLSM), LSM 510 (Carl Zeiss, Oberlochen, Germany). Microvessel density was quantified by counting the percentage area of CD31 positive pixels per image with at least 21 images per sample (i.e., three animals per sample x 7 cryosections per tumor).

2.5.6. Micelle accumulation in tumor tissue

Polyplex micelles loading Cy5-labeled pDNA were intravenously injected at a dose of 20 μg pDNA/mouse. Mice were sacrificed after 24 h and the excised tumors were fixed in formalin for 1 h, followed by 1 h incubation periods with 10, 15 and 20% sucrose/PBS solutions at room temperature. The tumors were frozen in tissue-Tek-OCT and cryosections were prepared for CLSM visualizations as described in the previous section. The nuclei were stained with Hoechst 33342 (Dojindo Lab., Kumamoto, Japan). The CLSM observations were performed at the excitation wavelengths of 488 nm (Ar laser) for the Alexa Fluor 488, 633 nm (He–Ne laser) for Cy5, and 710 nm (MaiTai laser, two photon excitation) for Hoechst 33342, respectively. The percentage of pDNA positive pixels per image was counted to quantify the micelle accumulation inside the tumor tissue.

2.6. Data analysis

The experimental data was analyzed by Student's *t*-test. $P<0.05$ was considered as significant.

3. Results

Thiolated acetal-PEG-PLys block copolymers, composed of 17 kDa M.W. PEG and 73 lysine units, were prepared as described elsewhere [12,14,37]. SPDP was used as a thiolating reagent and conjugated to the ε-amino group of lysine unit. Conjugation of c (RGDfK) peptide ligands into the PEG terminus of acetal-PEG-P(Lys-PDP) was achieved through the formation of a thiazolidine ring between the *N*-terminal cysteine and the aldehyde group converted from the acetal group [14,15]. The targetable polyplex micelles were prepared through ion complexation of the above polymers with pDNA at $N/P=2$ (Fig. 1), and analyzed for their size and ζ-potential by DLS and laser-doppler electrophorsis, respectively. The cumulant diameters of the B-SHX% micelles were approximately 104 ± 18 nm, with a moderate polydispersity index of 0.2. The ζ-potentials were found to be approximately 0.5 mV, as a result of the PEG palisade formation surrounding the polyplex core [8,14].

Following *in vitro* transfection in HeLa cells, the mRNA expressions of sFlt-1 were quantitatively analyzed by real time RT-PCR. From this analysis, presented in Fig. 2, it is clear that the cells were successfully transfected by the polyplex micelles. The highest transfection efficiency was achieved by RGD(+) B-SH15% crosslinked (15(+)) micelle. Worth noting, detectable protein level of sFlt-1 by ELISA, specific to human VEGF-R1/sFlt-1 (R&D Systems), could be achieved for this formulation only (1.2 ± 0.05 ng/mL) (data not shown). Other micelles, probably, resulted in sFlt-1 levels which are beyond the sensitivity of this assay (<13 pg/ml). The increased transfection efficiency of the 15(+) micelle results from the combination of crosslinked core and receptor targeting ligand, consistent with our previous studies [15].

The blood circulation experiments were carried out in BxPC3 tumor bearing mice upon intravenous injections of the Cy5-labeled pDNA (20 μg pDNA/ mouse). Blood was collected from the postcaval vein 15 min after administration and analyzed for its fluorescence intensity. Disulfide crosslinks prolonged blood circulation time, while the RGD conjugation resulted in significantly lower blood circulation period of polyplex micelles, as shown in Fig. 3. In the case of crosslinked system, 28% and 21% of injected pDNA were observed in plasma for RGD(−) and RGD(+) micelles, respectively. Significantly lower recovered doses of pDNA, 11 % and 7 % for RGD(−) and RGD(+) micelles, respectively, were found for non crosslinked system. We further evaluated micelle accumulation in tumor by iv administration of RGD-conjugated or non-conjugated 15% crosslinked micelles prepared with Cy5-labeled pDNA at a dose of 20 μg pDNA/mouse. Both micelles were found to be localized in the tumor blood vessels, 24 h after administration, as was indicated by colocalization of the Cy5-labeled pDNA (red) and the CD31 positive endothelial cells (green) (Fig. 4A). However, quantitative analysis of the pDNA positive area per image revealed significantly higher accumulation of the RGD-conjugated micelle than non-conjugated micelle inside the tumor tissue (Fig. 4B): 3.08 % and 2.44 % of red pixels per image for RGD(+) and RGD(−) micelle, respectively ($P<0.05$).

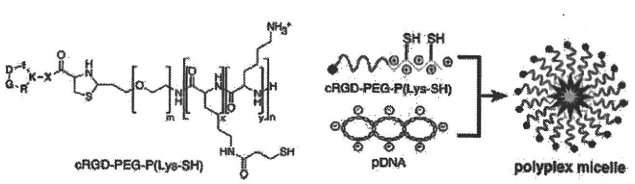

Fig. 1. Structure of cRGD-PEG-P(Lys-SH) and its polyplex micelle.

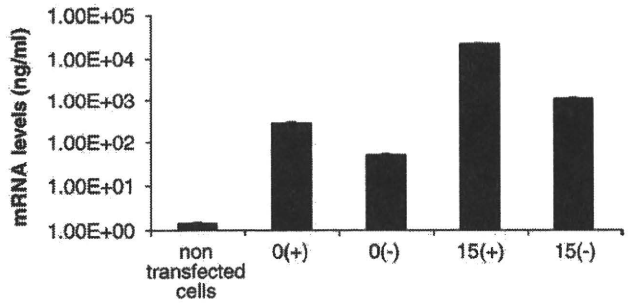

Fig. 2. *In vitro* transfection efficiency of sFlt-1 plasmid DNA in HeLa cells. The cells were transfected with RGD(+) and RGD(−) non crosslinked micelles (0(+) and 0(−)) and RGD(+) and RGD(−) 15% crosslinked micelles (15(+) and 15(−)), respectively. Non transfected cells were used as control. Each well was transfected with 1 μg of pDNA for 48 h and analyzed for sFlt-1 mRNA levels by real time RT-PCR.

The therapeutic effect of polyplex micelles following intravenous administration of the sFlt-1 expressing pDNA was evaluated by tumor growth inhibition study in BxPC3 tumor bearing mice. When tumors reached the volume of 120–160 mm^3, animals were injected with three doses of polyplex micelles containing either sFlt-1 or Luc expressing plasmid (20 μg pDNA/dose) on days 0, 4 and 8. The results of these studies, in terms of relative tumor volumes (Fig. 5), indicate the ability of RGD(+) and RGD(−) crosslinked polyplex micelles as vehicles for therapeutic gene delivery in BxPC3 tumor bearing mice. In the case of animals treated with 15(+) micelles, the tumor progression was significantly inhibited from day 6, compared to control mice. By the end of the experiment, the mean tumor volume in this group was 1.67 ± 0.18 of initial tumor volume. In the group of animals treated with pDNA encapsulated in RGD(−) micelles, significant inhibition of tumor progression was observed only from day 12, and the mean tumor volume reached 1.93 ± 0.52 of initial tumor volume by the end of the experiment. On the other hand, tumors grew much faster in the control groups, and reached 2.58 ± 0.5 of initial tumor volume.

Intravenous administration of crosslinked polyplex micelles containing sFlt-1 pDNA to BxPC3 tumor bearing mice resulted in significant reduction in the tumor neo-vasculature, as shown by CD31 immunostaining of the tumor cryosections. Representative images are shown in Fig. 6A. Increased density of blood vessels throughout the tissue was observed in control tumors. In contrast, very few blood vessels could be observed in the sFlt-1 treated groups. The quantitative results of microvessel density in tumor tissue cryosections were obtained by counting the area of stained blood vessels (green pixels) per image (Fig. 6B). Systemic administration of sFlt-1 expressing pDNA in the RGD(+) micelles resulted in the lowest average microvessel density of only 8.6% per image, whereas the RGD (−) micelle carrying pDNA led to 12.3% vessels per image. The control group had an average microvessel area of 23.7% per image, significantly higher as compared to the treated groups.

4. Discussion

In this study, we demonstrate that crosslinked polyplex micelles formed by electrostatic interaction of thiolated PEG-PLys block copolymers, modified on their surface with cRGD peptide ligand, and sFlt-1 pDNA are effective for *in vivo* tumor regression upon systemic administration. The thiolated PEG-PLys block copolymer, in this study, was further optimized by higher molecular weight PEG (17,000 Da) against 12,000 Da M.W. PEG used so far [2,3,8,12–15], to achieve enhanced shielding effect and thus higher stability in blood. Block copolymer with 15% thiolation degree, which showed the highest transfection efficiency *in vitro* and *in vivo* (data not shown), was selected for construction of RGD-mediated gene delivery vector.

The results of sFlt-1 transfection in Hela cells show higher mRNA expression levels in the cells transfected by RGD(+) crosslinked micelle relative to either RGD(−) or non crosslinked micelles (Fig. 2). This result is consistent with our previous studies, indicating the greater stability of crosslinked micelles in the medium and specific affinity of RGD ligand to $\alpha_v\beta_3$ and $\alpha_v\beta_5$ integrin receptors expressed in HeLa cells [14,15]. Micelle internalization to the cell via integrin-mediated endocytosis contributes to the accelerated accumulation of pDNA in the perinuclear region through the change in its intracellular trafficking from clathrin-mediated to caveolae-mediated endocytosis, resulting in enhancement of gene expression [15].

When administrated intravenously into BxPC3 tumor bearing mice, blood levels of Cy5-labeled pDNA were significantly lower for the RGD(+) micelle compared to the RGD(−) micelle. This observation might be partly explained by enhanced accumulation of pDNA in tumor site when carried by RGD(+) micelle over RGD(−) (Fig. 4B) and other organs as well. These observations are in good agreement with other works using cyclic RGD-modified particles, which reported significantly lower blood circulation times [38–40] while higher accumulation in tumor tissue [21,38–41], liver [21,38–42] and spleen [28–31] compared to the control. Moreover, CLSM observations demonstrated colocalization of both micelles with tumor endothelial cells, confirming their potential as effective antiangiogenic gene delivery vehicles (Fig. 4A).

In vivo tumor growth assay revealed significant ($P<0.05$) tumor growth inhibition when the sFlt-1 pDNA was administrated by crosslinked micelles as compared to control groups. Compared to RGD(−), the RGD(+) micelle was more effective in suppressing tumor growth. The significant difference in relative tumor volumes between RGD(+) injected and control groups was observed from day 6 till the end of the experiment. In comparison, significant difference between RGD(−) injected and control groups was observed only from day 12. In addition, relative tumor volumes in the RGD(+) injected group were lower than those in the RGD(−). These findings may be explained by greater tumor accumulation and higher transfection efficiency of RGD-modified micelle, resulted from more effective intracellular plasmid delivery through specific receptor binding and endocytosis. The lack of significant difference in relative tumor volumes between the RGD(+) and RGD(−) injected groups might be due to the lower circulation time in blood of the RGD(+) micelle and its enhanced accumulation in organs such as liver and spleen. Accumulation in liver [21,38–42] and spleen [39–42] was shown for various cyclic RGD-modified vectors and was, in general, attributed to their accelerated clearance through the phagocytosis by macrophages located on reticuloendothelial system (RES) [39–41].

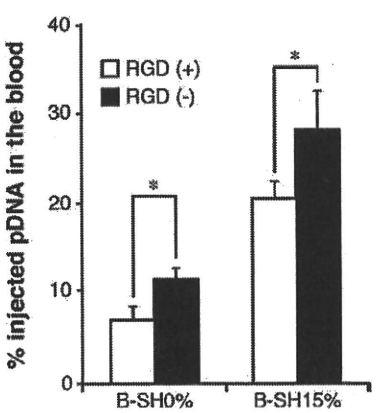

Fig. 3. Blood circulation of plasmid DNA carried by RGD (+/−) polyplex micelles. Micelles loading Cy5-labeled pDNA were intravenously administrated to the tumor bearing mice (20 μg pDNA/mouse). Blood was collected 15 min after administration and analyzed for its fluorescence intensity. $N=3$, Mean ± s.d. *$P<0.05$ compared to RGD(−).

The antiangiogenic effect of expressed sFlt-1 was confirmed by CD31 immunostaining of the tumor cryosections and quantification of microvessel density. From these studies, it is clear that sFlt-1 was able to significantly suppress tumor neo-vasculature formation when the pDNA was delivered in RGD(+) and RGD(−) crosslinked micelles. The most pronounced effect on microvessel density was observed with the plasmid administrated in RGD(+) micelles. This is probably due to the combined effect of tumor accumulation and increased transfection efficiency of the RGD-conjugated 15% crosslinked polyplex micelle.

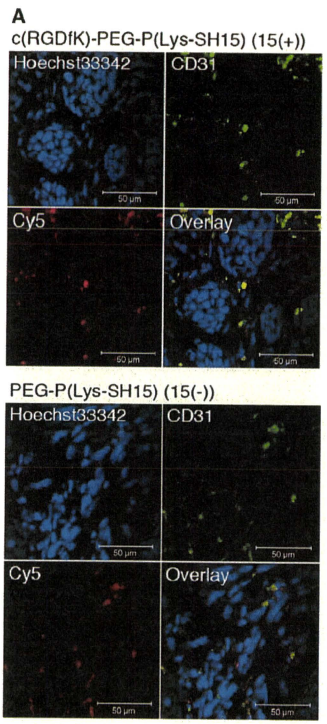

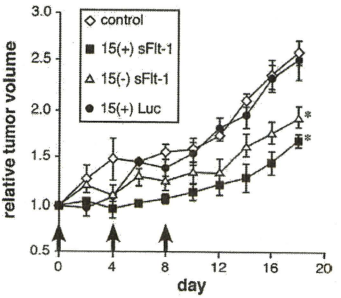

Fig. 5. *In vivo* tumor growth inhibition. RGD (+) and RGD (−) 15% crosslinked polyplex micelles loading plasmid DNA coding either sFlt-1 or Luc were administrated intravenously to BxPC3 tumor bearing mice at a pDNA dose of 20 μg on days 0, 4 and 8, as indicated by arrows. Control animals were injected with either Hepes buffer or 15 (+) micelle loading Luc expressing pDNA. Tumor volumes were measured every 2 days up to day 18 and normalized to the initial tumor volume (day 0). Results are presented in terms of relative tumor volumes, mean ± s.d., $N = 6$. $^*P < 0.05$ compared to control group.

5. Conclusion

Our data contributes to the list of successful non-viral systems for antiangiogenic cancer gene therapy utilizing sFlt-1 pDNA as VEGF sequester [21,35] and RGD targeting of tumor endothelial cells [19,21]. Worth noting, the antiangiogenic gene therapy by sFlt-1 pDNA, delivered by non-viral vector with cRGD ligand, appears to be a promising strategy to treat an intractable pancreatic tumor.

The significant inhibitory effect of tumor growth shown in this study, confirms the potential of c(RGDfK)-PEG-P(Lys-SH15) and PEG-P(Lys-SH15) polyplex micelles as effective systemic gene delivery systems to the neo-vasculature of solid tumors. Both of these formulations showed accumulation and interaction with tumor endothelial cells. The therapeutic activity of c(RGDfK)-PEG-P(Lys-SH15) was pronounced by combined effect of increased tumor accumulation and enhanced intracellular delivery. Based on these studies, c(RGDfK)-PEG-P(Lys-SH15) can be employed as an effective platform for systemic administration of therapeutic plasmid DNA for antiangiogenic therapy.

Acknowledgement

This work was financially supported in part by the Core Research Program for Evolutional Science and Technology (CREST) from Japan

Fig. 4. Micelle localization in tumor tissue. (A) Tumor endothelium and pDNA localization. Immunostaining of CD31 (green) revealed colocalization of Cy5-labeled pDNA (red) with tumor vasculature for both RGD-conjugated (15(+)) and non-conjugated (15(−)) micelles, 24 h after administration. The cell nuclei were stained with Hoechst 33342 (blue). (B) Quantitative analysis of Cy5-labeled pDNA (red pixels). The results represent percentage areas of pDNA-positive pixels per image. Seven images were taken from each tumor tissue, from 3 mice, mean ± s.d.

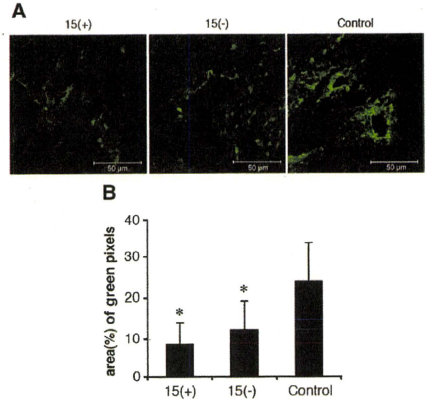

Fig. 6. Antiangiogenic effect of expressed sFlt-1 in BxPC3 tumor bearing mice. Tumor microvessels were detected by CD31 (PECAM1) antibody staining of tumor cryosections 20 days after therapy. (A) Representative CD31 immunostaining images. (B) Quantitative analysis of microvessel density in tumor cryosections. The results represent a percentage area of green pixels per image. Seven images were taken from each tumor tissue, from 3 mice, mean ± s.d. *$P<0.05$ compared to control group.

Science and Technology Agency (JST) as well as by Grants-in-Aid for Young Scientists (A). We express our appreciation to Prof. M. Shibuya (Tokyo Medical and Dental University) for providing pVL 1393 baculovirus vector pDNA encoding human sFlt-1. We thank Ms. S. Ogura (The University of Tokyo) for her technical assistance.

References

[1] A. Harada, K. Kataoka, Formation of polycation complex micelles in an aqueous milieu from a pair of oppositely-charged block copolymers with poly(ethylene glycol) segments, Macromolecules 28 (15) (1995) 5294–5299.
[2] S. Katayose, K. Kataoka, Water-soluble polyion complex associates of DNA and poly(ethylene glycol)-poly(L-lysine) block copolymer, Bioconjug. Chem. 8 (5) (1997) 702–707.
[3] M. Harada-Shiba, K. Yamauchi, A. Harada, I. Takamisawa, K. Shimokado, K. Kataoka, Polyion complex micelles as vectors in gene therapy — pharmacokinetics and in vivo gene transfer, Gene Ther. 9 (6) (2002) 407–414.
[4] M. Laus, K. Sparnacci, B. Ensoli, S.O. Buttò, A. Caputo, I. Mantovani, G. Zuccheri, B. Samorì, L. Tondelli, Complex associates of plasmid DNA and a novel class of block copolymers with PEG and cationic segments as new vectors for gene delivery, J. Biomater. Sci. Polym. Ed. 12 (2) (2001) 209–228.
[5] C.H. Ahn, S.Y. Chae, Y.H. Bae, S.W. Kim, Synthesis of biodegradable multi-block copolymers of poly(L-lysine) and poly(ethylene glycol) as a non-viral gene carrier, J. Control. Release 97 (3) (2004) 567–574.
[6] Y. Wang, C.Y. Ke, B.C. Weijie, S.Q. Liu, S.H. Goh, Y.Y. Yang, The self-assembly of biodegradable cationic polymer micelles as vectors for gene transfection, Biomaterials 28 (35) (2007) 5358–5368.
[7] Y.R. Choi, S.Y. Chae, C.H. Ahn, M. Lee, S. Oh, Y. Byun, B.D. Rhee, K.S. Ko, Development of polymeric gene delivery carriers: PEGylated copolymers of L-lysine and L-phenylalanine, J. Drug Target. 15 (6) (2007) 391–398.
[8] K. Itaka, K. Yamauchi, A. Harada, K. Nakamura, H. Kawaguchi, K. Kataoka, Polyion complex micelles from plasmid DNA and poly(ethylene glycol)-poly(L-lysine) block copolymer as serum-tolerable polyplex system: physicochemical properties of micelles relevant to gene transfection efficiency, Biomaterials 24 (24) (2003) 4495–4506.
[9] S. Mishra, P. Webster, M.E. Davis, PEGylation significantly affects cellular uptake and intracellular trafficking of non-viral gene delivery particles, Eur. J. Cell Biol. 83 (3) (2004) 97–111.
[10] A.M. Funhoff, S. Monge, R. Teeuwen, G.A. Koning, N.M. Schuurmans-Nieuwenbroek, D.J. Crommelin, D.M. Haddleton, W.E. Hennink, C.F. van Nostrum, PEG shielded polymeric double-layered micelles for gene delivery, J. Control. Release 102 (3) (2005) 711–724.
[11] H.K. de Wolf, C.J. Snel, F.J. Verbaan, R.M. Schiffelers, W.E. Hennink, G. Storm, Effect of cationic carriers on the pharmacokinetics and tumor localization of nucleic acids after intravenous administration, Int. J. Pharm. 331 (2) (2007) 167–175.
[12] K. Miyata, Y. Kakizawa, N. Nishiyama, A. Harada, Y. Yamasaki, H. Koyama, K. Kataoka, Block catiomer polyplexes with regulated densities of charge and disulfide cross-linking directed to enhance gene expression, J. Am. Chem. Soc. 126 (8) (2004) 2355–2361.
[13] K. Miyata, Y. Kakizawa, N. Nishiyama, Y. Yamasaki, T. Watanabe, M. Kohara, K. Kataoka, Freeze-dried formulations for in vivo gene delivery of PEGylated polyplex micelles with disulfide crosslinked cores to the liver, J. Control. Release 109 (1–3) (2005) 15–23.
[14] M. Oba, S. Fukushima, N. Kanayama, K. Aoyagi, N. Nishiyama, H. Koyama, K. Kataoka, Cyclic RGD peptide-conjugated polyplex micelles as a targetable gene delivery system directed to cells possessing $\alpha_v\beta_3$ and $\alpha_v\beta_5$ integrins, Bioconjug. Chem. 18 (5) (2007) 1415–1423.
[15] M. Oba, K. Aoyagi, K. Miyata, Y. Matsumoto, K. Itaka, N. Nishiyama, Y. Yamasaki, H. Koyama, K. Kataoka, Polyplex Micelles with cyclic RGD peptide ligands and disulfide cross-links directing to the enhanced transfection via controlled intracellular trafficking, Mol. Pharmaceutics 5 (6) (2008) 1080–1092.
[16] M.D. Pierschbacher, E. Ruoslahti, Cell attachment activity of fibronectin can be duplicated by small synthetic fragments of the molecule, Nature 309 (5963) (1984) 30–33.
[17] R. Haubner, R. Gratias, B. Diefenbach, S.L. Goodman, A. Jonczyk, H. Kessler, Structural and functional aspects of RGD-containing cyclic pentapeptides as highly potent and selective integrin $\alpha_v\beta_3$ antagonists, J. Am. Chem. Soc. 118 (1996) 7461–7472.
[18] A. Erdreich-Epstein, H. Shimada, S. Groshen, M. Liu, L.S. Metelitsa, K.S. Kim, M.F. Stins, R.C. Seeger, D.L. Durden, Integrins alpha(v)beta3 and alpha(v)beta5 are expressed by endothelium of high-risk neuroblastoma and their inhibition is associated with increased endogenous ceramide, Cancer Res. 60 (3) (2000) 712–721.
[19] R.M. Schiffelers, A. Ansari, J. Xu, Q. Zhou, Q. Tang, G. Storm, G. Molema, P.Y. Lu, P.V. Scaria, M.C. Woodle, Cancer siRNA therapy by tumor selective delivery with ligand-targeted sterically stabilized nanoparticle, Nucleic Acids Res. 32 (19) (2004) e149.
[20] W.J. Kim, J.W. Yockman, M. Lee, J.H. Jeong, Y.H. Kim, S.W. Kim, Soluble Flt-1 gene delivery using PEI-g-PEG-RGD conjugate for anti-angiogenesis, J. Control. Release 106 (1–2) (2005) 224–234.
[21] W.J. Kim, J.W. Yockman, J.H. Jeong, L.V. Christensen, M. Lee, Y.H. Kim, S.W. Kim, Anti-angiogenic inhibition of tumor growth by systemic delivery of PEI-g-PEG-RGD/pCMV-sFlt-1 complexes in tumor-bearing mice, J. Control. Release 114 (3) (2006) 381–388.
[22] K. Temming, R.M. Schiffelers, G. Molema, R.J. Kok, RGD-based strategies for selective delivery of therapeutics and imaging agents to the tumor vasculature, Drug Resist. Updat. 8 (6) (2005) 381–402.
[23] K.A. Thomas, Vascular endothelial growth factor, a potent and selective angiogenic agent, J. Biol. Chem. 271 (2) (1996) 603–606.
[24] G. Breier, Functions of the VEGF/VEGF receptor system in the vascular system, Semin. Thromb. Hemost. 26 (5) (2000) 553–559.
[25] R.A. Brekken, P.E. Thorpe, VEGF-VEGF receptor complexes as markers of tumor vascular endothelium, J. Control. Release 74 (1–3) (2001) 173–181.
[26] A.L. Harris, Anti-angiogenesis therapy and strategies for integrating it with adjuvant therapy, Recent Results Cancer Res. 152 (1998) 341–352.
[27] N. Ferrara, VEGF as a therapeutic target in cancer, Oncology 69 (2005) 11–16.
[28] R.L. Kendall, G. Wang, K.A. Thomas, Identification of a natural soluble form of the vascular endothelial growth factor receptor, FLT-1, and its heterodimerization with KDR, Biochem. Biophys. Res. Commun. 226 (2) (1996) 324–328.
[29] H. Chen, U. Ikeda, M. Shimpo, Y. Maeda, M. Shibuya, K. Ozawa, K. Shimada, Inhibition of vascular endothelial growth factor activity by transfection with the soluble FLT-1 gene, J. Cardiovasc. Pharmacol. 36 (4) (2000) 498–502.
[30] M. Malecki, H. Trembacz, B. Szaniawska, M. Przybyszewska, P. Janik, Vascular endothelial growth factor and soluble FLT-1 receptor interactions and biological implications, Oncol. Rep. 14 (6) (2005) 1565–1569.
[31] C. Ye, C. Feng, S. Wang, K.Z. Wang, N. Huang, X. Liu, Y. Lin, M. Li, sFlt-1 gene therapy of follicular thyroid carcinoma, Endocrinology 145 (2) (2004) 817–822.
[32] Y. Hasumi, H. Mizukami, M. Urabe, T. Kohno, K. Takeuchi, A. Kume, M. Momoeda, H. Yoshikawa, T. Tsuruo, M. Shibuya, Y. Taketani, K. Ozawa, Soluble FLT-1 expression suppresses carcinomatous ascites in nude mice bearing ovarian cancer, Cancer Res. 62 (7) (2002) 2019–2023.
[33] G. Mahendra, S. Kumar, T. Isayeva, P.J. Mahasreshti, D.T. Curiel, C.R. Stockardt, W.E. Grizzle, V. Alapati, R. Singh, G.P. Siegal, S. Meleth, S. Ponnazhagan, Antiangiogenic cancer gene therapy by adeno-associated virus 2-mediated stable expression of the soluble FMS-like tyrosine kinase-1 receptor, Cancer Gene Ther. 12 (1) (2005) 26–34.
[34] Y. Takei, H. Mizukami, Y. Saga, I. Yoshimura, Y. Hasumi, T. Takayama, T. Kohno, T. Matsushita, T. Okada, A. Kume, M. Suzuki, K. Ozawa, Suppression of ovarian cancer by muscle-mediated expression of soluble VEGFR-1/Flt-1 using adeno-associated virus serotype 1-derived vector, Int. J. Cancer 120 (2) (2007) 278–284.
[35] S. Kommareddy, M. Amiji, Antiangiogenic gene therapy with systemically administered sFlt-1 plasmid DNA in engineered gelatin-based nanovectors, Cancer Gene Ther. 14 (5) (2007) 488–498.
[36] M.R. Kano, Y. Komuta, C. Iwata, M. Oka, Y.T. Shirai, Y. Morishita, Y. Ouchi, K. Kataoka, K. Miyazono, Comparison of the effects of the kinase inhibitors imatinib, sorafenib, and transforming growth factor-beta receptor inhibitor on extravasation of nanoparticles from neovasculature, Cancer Sci. 100 (1) (2009) 173–180.
[37] A. Harada, K. Kataoka, Formation of polyion complex micelles in an aqueous milieu from a pair of oppositely charged block copolymers with poly(ethylene glycol) segments, Macromolecules 28 (1995) 294–299.

[38] P.K. Dubey, V. Mishra, S. Jain, S. Mahor, S.P. Vyas, Liposomes modified with cyclic RGD peptide for tumor targeting, J. Drug Target. 12 (5) (2004) 257–264.
[39] A.J. Schraa, R.J. Kok, H.E. Moorlag, E.J. Bos, J.H. Proost, D.K. Meijer, L.F. de Leij, G. Molema, Targeting of RGD-modified proteins to tumor vasculature: a pharmacokinetic and cellular distribution study, Int. J. Cancer 102 (5) (2002) 469–475.
[40] R.M. Schiffelers, G.A. Koning, T.L. ten Hagen, M.H. Fens, A.J. Schraa, A.P. Janssen, R.J. Kok, G. Molema, G. Storm, Anti-tumor efficacy of tumor vasculature-targeted liposomal doxorubicin, J. Control. Release 91 (1–2) (2003) 115–122.
[41] A. Mitra, J. Mulholland, A. Nan, E. McNeill, H. Ghandehari, B.R. Line, Targeting tumor angiogenic vasculature using polymer-RGD conjugates, J. Control. Release 102 (1) (2005) 191–201.
[42] D.C. Bibby, J.E. Talmadge, M.K. Dalal, S.G. Kurz, K.M. Chytil, S.E. Barry, D.G. Shand, M. Steiert, Pharmacokinetics and biodistribution of RGD-targeted doxorubicin-loaded nanoparticles in tumor-bearing mice, Int. J. Pharm. 293 (1–2) (2005) 281–290.

DRUG DELIVERY

Improving Drug Potency and Efficacy by Nanocarrier-Mediated Subcellular Targeting

Mami Murakami,[1] Horacio Cabral,[1,2] Yu Matsumoto,[3] Shourong Wu,[3] Mitsunobu R. Kano,[4] Takao Yamori,[5] Nobuhiro Nishiyama,[2,3]* Kazunori Kataoka[1,2,3,6]*

Nanocarrier-mediated drug targeting is an emerging strategy for cancer therapy and is being used, for example, with chemotherapeutic agents for ovarian cancer. Nanocarriers are selectively accumulated in tumors as a result of their enhanced permeability and retention of macromolecules, thereby enhancing the antitumor activity of the nanocarrier-associated drugs. We investigated the real-time subcellular fate of polymeric micelles incorporating (1,2-diaminocyclohexane) platinum(II) (DACHPt/m), the parent complex of oxaliplatin, in tumor tissues by fluorescence-based assessment of their kinetic stability. These observations revealed that DACHPt/m was extravasated from blood vessels to the tumor tissue and dissociated inside each cell. Furthermore, DACHPt/m selectively dissociated within late endosomes, enhancing drug delivery to the nearby nucleus relative to free oxaliplatin, likely by circumvention of the cytoplasmic detoxification systems such as metallothionein and methionine synthase. Thus, these drug-loaded micelles exhibited higher antitumor activity than did oxaliplatin alone, even against oxaliplatin-resistant tumors. These findings suggest that nanocarriers targeting subcellular compartments may have considerable benefits in clinical applications.

INTRODUCTION

In 2009, about 10 million people worldwide were newly diagnosed with cancer (*1*). Application of nanotechnology to cancer therapy may offer therapeutic effects that cannot be achieved with other strategies. The main aim of this approach is to develop nanoscale drug vehicles for targeted cancer therapy (*2–5*). Nanocarriers selectively accumulate in solid tumors as a result of the enhanced permeability and retention (EPR) effect, which is characterized by microvascular hyperpermeability to circulating macromolecules and impaired lymphatic drainage in tumor tissues (*6*). At present, several nanocarrier formulations have been approved for clinical use against ovarian cancer and HIV-associated Kaposi's sarcoma (Doxil) and breast cancer (Abraxane). These formulations allow better accumulation of the drugs doxorubicin and paclitaxel in tumors (*7*).

Polymeric micelles, self-assemblies of block copolymers, have gained increasing popularity as tumor-targetable nanocarriers since they were first used as drug vehicles in the late 1980s (*8–12*). These micelles, which are several tens of nanometers in size and have a characteristic core-shell structure consisting of a drug-loaded hydrophobic core and poly(ethylene glycol) (PEG) hydrophilic shell, are long-lived in the bloodstream and effectively accumulate in solid tumors after intravenous injection (*8*). The critical features of polymeric micelles for their function as drug vehicles, including size, drug loading and release, and specific binding to the target cells, can be modulated by engineering the constituent block copolymers. At present, our micelle formulations incorporating doxorubicin, paclitaxel, SN-38, cisplatin, and (1,2-diaminocyclohexane) platinum(II) (DACHPt) are undergoing clinical trials (development code names NK911, NK105, NK012, NC-6004, and NC-4016, respectively), and four of these have advanced to Phase II studies (*13–17*). These clinical studies have revealed that polymeric micelles reduce side effects from the incorporated drugs and are effective against various intractable tumors, such as triple-negative breast cancers (*18*), indicating their clinical potential.

Recently, increasing attention has been paid to another potentially useful property of nanocarriers: to achieve subcellular drug targeting. Subcellular drug targeting of nanocarriers could enhance the pharmacological activity of the loaded drugs through improved subcellular drug distribution (*19*). Drug vehicles designed to release active drugs in acidic organelles, such as the endosome and lysosome, can circumvent recognition by the drug efflux pump (for example, P-glycoprotein) through internalization by endocytosis, thus overcoming multidrug resistance in cancer cells (*20–22*). Here, we aimed to investigate the potential of DACHPt-loaded micelles (DACHPt/m) for in vivo subcellular targeting. DACHPt/m is formed by the polymer-metal complexation between DACHPt and the carboxylic group of poly(ethylene glycol)-*b*-poly(glutamic acid) [PEG-*b*-P(Glu)] copolymers. DACHPt is the parent complex of the clinically approved drug oxaliplatin. Oxaliplatin has a hydrolyzable oxalate group to increase its solubility in water, which can be removed by nucleophiles in biological media, such as chloride ions. Aqua complexes ($[(DACH)Pt(H_2O)Cl]^+$ or $[(DACH)Pt(H_2O)_2]^{2+}$) of DACHPt exhibit chemotherapeutic activity. DACHPt/m releases DACHPt and the micelle structure dissociates depending on the pH and chloride ion concentrations, a result of ligand substitution of the Pt(II) from the carboxylates in the micelle core with the chloride ions in the medium (Fig. 1A) (*23*, *24*). Moreover, after DACHPt/m is internalized into cancer cells, it would be expected to be exposed to different pH and chloride ion concentrations during subcellular trafficking (*25*). We hypothesized that DACHPt/m would be selectively released in low-pH cellular compartments, bypassing

[1]Department of Bioengineering, Graduate School of Engineering, University of Tokyo, 7-3-1 Hongo, Bunkyo-ku, Tokyo 113-8656, Japan. [2]Center for NanoBio Integration, University of Tokyo, Tokyo 113-8656, Japan. [3]Center for Disease Biology and Integrative Medicine, Graduate School of Medicine, University of Tokyo, Tokyo 113-0033, Japan. [4]Department of Molecular Pathology, Graduate School of Medicine, University of Tokyo, Tokyo 113-0033, Japan. [5]Division of Molecular Pharmacology, Cancer Chemotherapy Center, Japanese Foundation for Cancer Research, 3-10-6 Ariake, Koto-ku, Tokyo 135-8550, Japan. [6]Department of Materials Engineering, Graduate School of Engineering, University of Tokyo, Tokyo 113-8656, Japan.
*To whom correspondence should be addressed. E-mail: nishiyama@bmw.t.u-tokyo.ac.jp (N.N.); kataoka@bmw.t.u-tokyo.ac.jp (K.K.)

cytoplasmic detoxification and thereby improving potency and efficacy (Fig. 1B). Indeed, we previously reported that cisplatin-loaded micelles, which are formed in the same manner as DACHPt/m, caused different gene expression patterns than did cisplatin alone because of their different internalization pathways and the facilitated drug release in endosomes and lysosomes (*26*). To test the above-mentioned hypothesis, we constructed fluorescent-labeled DACHPt/m (F-DACHPt/m) with a dual fluorescent-labeling method so that we could follow the intracellular localization and dissociation of the micelles by using in vivo confocal microscopy, and intravitally evaluated the extravasation, penetration, cellular uptake, and subcellular fate of DACHPt/m in tumor tissues and their activity against human colorectal cancers.

RESULTS

Construction and characterization of F-DACHPt/m

To construct the dual fluorescent-labeled block copolymer, we conjugated the fluorescent dyes boron dipyrromethene (BODIPY) FL (excitation wavelength, 503 nm; emission wavelength, 512 nm) and BODIPY TR (excitation wavelength, 588 nm; emission wavelength, 616 nm) to the α- and ω-end groups of α-4-(diethoxymethyl)benzyl-poly(ethylene glycol)-*b*-poly(L-glutamic acid), respectively, and thus obtained BODIPY FL-PEG-*b*-P(Glu)-BODIPY TR (fig. S1). The conjugation degree for BODIPY FL to the block copolymer was 0.2 mol BODIPY FL per mole of polymer and for BODIPY TR was about 0.8 mol BODIPY TR per mole of polymer. We built F-DACHPt/m by the formation of polymer-metal complexes between DACHPt and the carboxylic groups of poly(glutamic acid) in BODIPY FL-PEG-*b*-P(Glu)-BODIPY TR (Fig. 1A). F-DACHPt/m had a diameter of 30 nm, similar to that of DACHPt/m (fig. S2). The intact F-DACHPt/m emitted fluorescence only from the shell-conjugated dye (BODIPY FL) because the core-conjugated dye (BODIPY TR) was quenched owing to its high local concentration. The close proximity of BODIPY TR fluorophores in the core of the micelles leads to self-quenching by the formation of nonfluorescent ground-state BODIPY TR dimers (or higher aggregates) (*27*). When DACHPt is released as a result of the ligand substitution of the Pt(II) from the carboxylates in the micelle core with the chloride in the medium, the density of the micelle core is reduced and the fluorescence of BODIPY TR is dequenched (Fig. 1A). We investigated the release of DACHPt from F-DACHPt/m and the fluorescence of BODIPY FL and BODIPY TR at the surface and core of the micelles, respectively, under conditions that mimicked the extracellular medium (pH 7.4 and 150 mM Cl^-), early endosomes (pH 6.9 and 20 mM Cl^-), and late endosomes and lysosomes (pH 5.5 and 70 mM Cl^-) (*25*). The fluorescence from BODIPY FL on the shell of the micelles was constant regardless of the pH and salt concentration of the media (Fig. 2, A to C, middle columns), suggesting that the fluorescence from BODIPY FL can be used to trace the position of the micelles in the biological environment. In addition, the drug release profile of F-DACHPt/m was similar to that of unmodified DACHPt/m, suggesting the feasibility of a direct comparison (Fig. 2, A to C, left columns). Under extracellular conditions, BODIPY TR fluorescence increased after an incubation period of 17 hours, simultaneous with the release of DACHPt from F-DACHPt/m (Fig. 2A). The release of DACHPt from F-DACHPt/m in the late endosomal conditions was considerably faster (Fig. 2C) than in the extra-

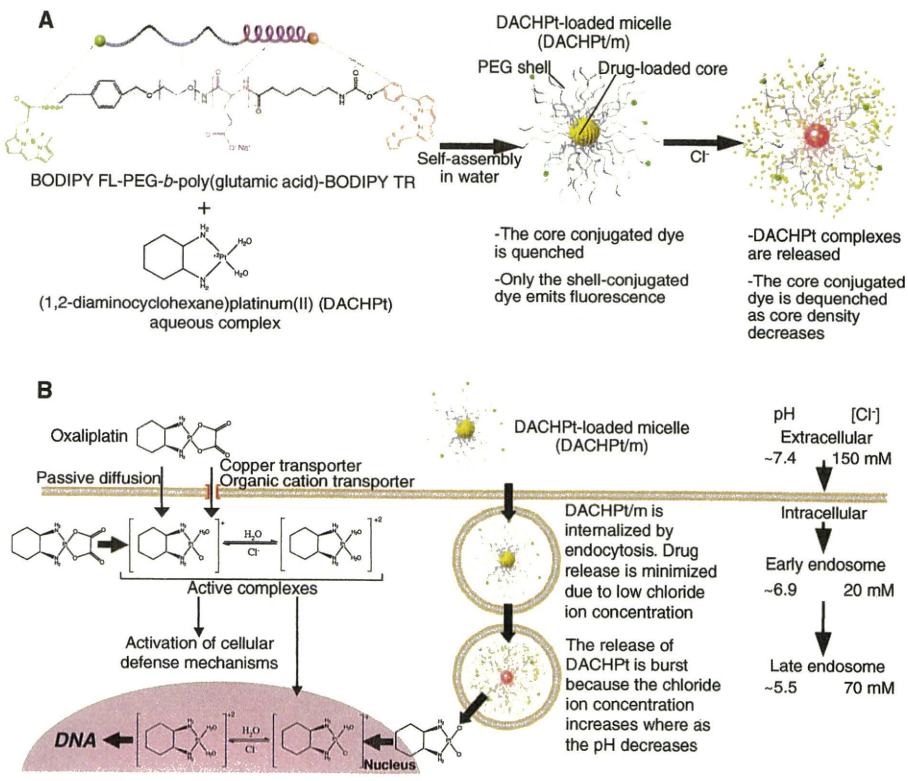

Fig. 1. Design of fluorescent-labeled DACHPt/m (F-DACHPt/m) for visualization of the localization and drug release in the cell. (**A**) F-DACHPt/m self-assembled through polymer-metal complex formation between DACHPt and boron dipyrromethene (BODIPY) FL–poly(ethylene glycol)-*b*-poly(glutamic acid)–BODIPY TR in distilled water. In the micelle state, only BODIPY FL (green) emits fluorescence, whereas BODIPY TR (red) remains quenched. As DACHPt is released from F-DACHPt/m in chloride ion–containing media, BODIPY TR is dequenched and emits fluorescence. (**B**) Schematic representation of hypothetical subcellular pathways and action of DACHPt/m. Oxaliplatin enter cells by passive diffusion or through copper/organic cation transporters. Once oxaliplatin is in the cytoplasm, most of the activated aqua species ($[(DACH)Pt(H_2O)Cl]^+$ or $[(DACH)Pt(H_2O)_2]^{2+}$) are eliminated by cellular detoxification mechanisms, but a small fraction binds to DNA. In contrast, DACHPt/m that enters tumor cells by endocytosis (middle) is exposed to an environment with increasing acidity and chloride ion concentration because early endosomes mature into the late endosomes. Drug release from DACHPt/m is accelerated in the late endosomal environment close to the perinuclear region, resulting in enhanced efficiency of drug delivery to the nucleus.

cellular and early endosomal conditions (Fig. 2, A and B), occurring without any delay. Further, mirroring the DACHPt release, F-DACHPt/m exhibited more robust fluorescence recovery of BODIPY TR under the late endosomal conditions (Fig. 2C) than under the early endosomal conditions (Fig. 2B, right columns). Thus, the fluorescence profiles of BODIPY TR are correlated with the release profiles of DACHPt from the micelles.

In vitro subcellular trafficking of F-DACHPt/m

The cellular internalization and fate of F-DACHPt/m in human tumor-derived colorectal cancer (HT29) cells, which are the most frequently used cell lines in oxaliplatin studies (*28*), were observed with time-lapse confocal laser scanning microscopy (CLSM) (Fig. 3A and video S1). The intensity of BODIPY FL fluorescence increased slightly over time (Fig. 3B), and the BODIPY FL fluorescence in the images was clearly visible within a 6-hour incubation (Fig. 3A). Meanwhile, with time, the intensity of BODIPY TR fluorescence continuously increased to a greater extent than did that of BODIPY FL fluorescence (Fig. 3B), and the BODIPY TR fluorescence in the images became visible at about 24 hours of incubation (Fig. 3A). This continuous increase in the intensity of BODIPY TR fluorescence corresponds to the dequenching of BODIPY TR fluorescence driven by the release of DACHPt in the cell. These results suggest that F-DACHPt/m enters the cells as a micelle form and then dissociates within the subcellular environments.

Using CLSM with higher magnification, we further evaluated the detailed subcellular trafficking and fate of F-DACHPt/m by focusing on individual cells. We confirmed that the micelles entered the cancer cells via endocytosis by incubating the cells with F-DACHPt/m at 37°C and 4°C. As endocytosis ceases at 4°C, the fluorescent signal of F-DACHPt/m inside the cells was undetectable, whereas at 37°C, the fluorescence from F-DACHPt/m was observed inside the cells (fig. S3). To examine the subcellular trafficking of the micelles, we determined the colocalization of BODIPY FL fluorescence from F-DACHPt/m with an early endosome marker, Rab5a-RFP, and a late endosome and lysosome marker, LysoTracker, in HT29 cells (Fig. 3C). Note that individual vesicular organelles can be recognized as punctate fluorescence in the images. After a 6-hour incubation at 37°C, BODIPY FL colocalized mainly with Rab5a-RFP (yellow fluorescence in Fig. 3C, upper images) rather than with LysoTracker. After prolonged incubation (24 and 55 hours), BODIPY FL showed decreased colocalization with Rab5a-RFP and increased colocalization with LysoTracker (yellow fluorescence in Fig. 3C, lower images). This observation was confirmed by quantification of colocalized fluorescent intensities of BODIPY FL with Rab5a-RFP or LysoTracker (Fig. 3D). These results suggested that the micelles might localize mainly in the early endosome until 6 hours and then move into the late endosome/lysosome compartment. Furthermore, we studied the timing and location of the micelle dissociation and concomitant drug release by evaluating the colocalization of F-DACHPt/m with LysoTracker (Fig. 3E and fig. S4A) and the quantification of BODIPY FL and BODIPY TR fluorescent intensities (fig. S4B), as well as the colocalization ratio (Fig. 3F). The fluorescence intensity from BODIPY FL gradually increased (fig. S4B). Meanwhile, the fluorescence of BODIPY TR became visible after 24-hour incubation (Fig. 3E and fig. S4A) and then increased over time (fig. S4B). Both BODIPY FL and BODIPY TR colocalized with LysoTracker (Fig. 3E and fig. S4A), and the colocalization ratio between BODIPY FL or BODIPY TR and LysoTracker increased over time (Fig. 3F). These observations sug-

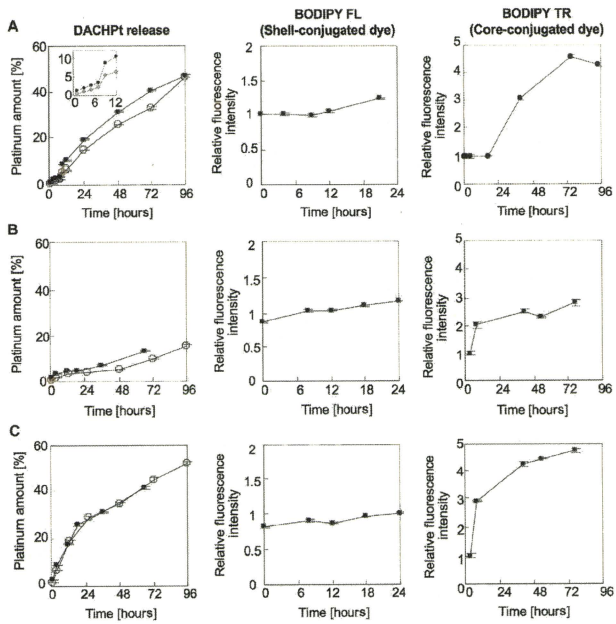

Fig. 2. Properties of F-DACHPt/m under conditions mimicking extracellular and subcellular environments. (**A** to **C**) Release profiles of DACHPt from DACHPt/m and F-DACHPt/m (left column) and fluorescence profiles of BODIPY FL (middle column) and BODIPY TR (right column) under conditions mimicking (A) the extracellular environment (10 mM PBS, pH 7.4, and 150 mM NaCl), (B) the early endosomal environment (10 mM PBS, pH 6.9, and 20 mM NaCl), and (C) the late endosomal environment (10 mM PBS, pH 5.5, and 70 mM NaCl), all at 37°C. Inset in top left panel is the magnification of the profiles of DACHPt release until 12 hours. The release of DACHPt from the micelles was evaluated by dialysis as described in Materials and Methods. Data for DACHPt/m and F-DACHPt/m in the left column are shown as open and filled circles, respectively. Data are expressed as means ± SEM ($n = 3$).

gested that F-DACHPt/m progressively dissociated in the late endosome and lysosomal compartments. Because these acidic organelles reside in the perinuclear region, F-DACHPt/m would be expected to deliver the active platinum complexes close to the nucleus. Thus, in vitro confocal microscopy revealed that F-DACHPt/m appears to exhibit late endosome/lysosome–selective dissociation concomitant with the release of DACHPt, thereby achieving efficient DACHPt delivery close to the nucleus.

Effect of subcellular pathway on drug efficiency

Oxaliplatin enters the cells by passive diffusion or through copper/organic cation transporters (*29*), and it then changes to active DACHPt aqua complexes in the cytoplasm, some of which may ultimately cross-link with DNA, disrupting DNA function and exerting therapeutic activity (Fig. 1B). However, 75 to 85% of activated platinum drugs are sequestered by abundant sulfur species that serve as cellular defense mechanisms in the cytoplasm, and only 5 to 10% of oxaliplatin can bind to DNA (Fig. 1B) (*30*–*32*). We hypothesized that DACHPt/m facilitates drug delivery close to the nucleus through its perinuclear subcellular localization. Therefore, we studied the pharmacological activity of DACHPt/m. DACHPt/m displayed a value of IC_{50} (the mean concentration that causes 50% growth inhibition) against HT29 cells that was lower than that of oxaliplatin by a factor of 4.7 (Table 1). It is rare that a nanocarrier-encapsulated drug surpasses the free form of the drug for in vitro cytotoxicity (*33*). To elucidate the mechanism of DACHPt/m action, we evaluated the subcellular accumulation of platinum and quantity of Pt-DNA adducts. Exposure of HT29 cells to oxaliplatin resulted in twice as much accumulation of platinum than did exposure to DACHPt/m (Fig. 3G). This is probably because oxaliplatin rapidly enters the cells by diffusion and through copper/organic cation transporters (*29*), whereas DACHPt/m is gradually internalized by endocytosis. Nevertheless, we did not observe a significant difference in the Pt-DNA adducts formed after exposure to oxaliplatin and DACHPt/m (Fig. 3H), indicating that DACHPt/m may efficiently deliver the active platinum drug to DNA (Fig. 3I).

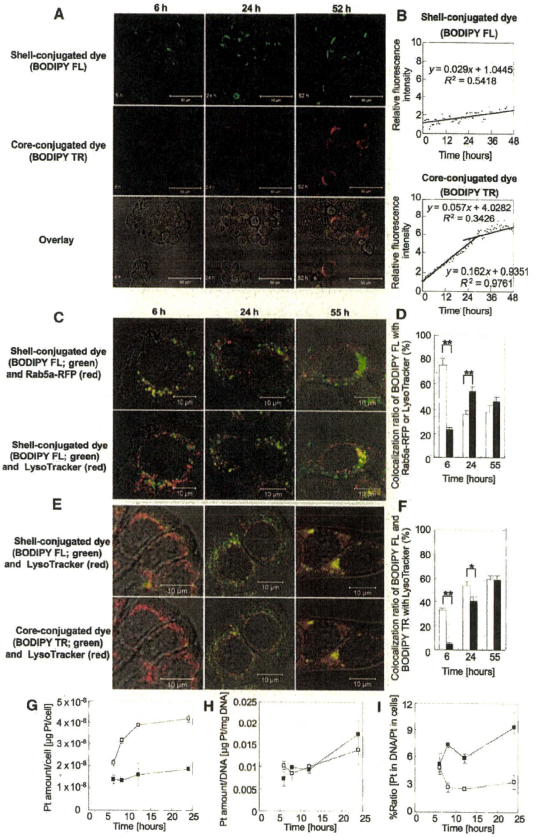

Fig. 3. In vitro observation of subcellular trafficking and fate of F-DACHPt/m, cellular platinum accumulation, and formation of platinum-DNA adducts. (**A**) Representative images of time-lapse CLSM observation of HT29 cells treated with F-DACHPt/m (green, BODIPY FL; red, BODIPY TR; yellow, their colocalization). (**B**) Relative fluorescence intensity of BODIPY FL (upper) and BODIPY TR (lower) of F-DACHPt/m. (**C**) Fluorescent images of colocalization of BODIPY FL of DACHPt/m (green) with an early endosome marker, Rab5a-RFP (red in upper images), or a late endosome and lysosome marker, LysoTracker (red in lower images), in HT29 cells after incubation for 6, 24, and 55 hours. (**D**) Colocalization ratio of BODIPY FL with Rab5a-RFP (open bars) or LysoTracker (closed bars). Data are expressed as means ± SEM ($n = 10$). $^{**}P < 0.01$. (**E**) Fluorescent images of colocalization of BODIPY FL (green in upper images) and BODIPY TR (green in lower images) of F-DACHPt/m with LysoTracker (red) in HT29 cells after incubation for 6, 24, and 55 hours. (**F**) Colocalization ratio of BODIPY FL (open bars) or BODIPY TR (closed bars) with LysoTracker. Data are expressed as means ± SEM ($n = 10$). $^{*}P < 0.05$; $^{**}P < 0.01$. (**G**) In vitro cellular accumulation of platinum. (**H**) DNA platination. (**I**) Ratio of platinum in DNA to total platinum in cells expressed as a percentage. DNA platination was converted from μg Pt/mg DNA to μg Pt/cell, and the ratio was calculated. Open squares, oxaliplatin; filled squares, DACHPt/m. Data are expressed as means ± SEM ($n = 3$).

We also evaluated the mean concentration required for 50% growth inhibition (GI_{50}), which is defined as in (*34*, *35*), in a human cell panel composed of 37 cancer cell lines (fig. S5), and investigated the correlation between GI_{50} and expression of 26 genes that we selected on the basis of their potential association with the pharmacological activity of platinum compounds (*36*). The cytotoxic activity of oxaliplatin was inversely correlated with the expression of metallothionein (MT1Q) and methionine synthase (MTR), which are found in the cytoplasm and inactivate platinum compounds. DACHPt/m cytotoxicity did not exhibit similar correlations (table S1). We conclude that DACHPt/m may bypass cytoplasmic detoxification by MTR and MT1Q and efficiently deliver active platinum complexes to the nucleus, because they are internalized by endocytosis and selectively release the active platinum complexes in the late endosome/lysosome compartment (Fig. 1B).

Effect of DACHPt/m on oxaliplatin resistance in vitro

Our proposed mechanism of action of DACHPt/m led us to investigate their efficacy in oxaliplatin-resistant cancer cells, because MTR and MT1Q are overexpressed in these cells (*37*–*39*). We developed oxaliplatin-resistant HT29 cells (HT29/ox) by chronic exposure of HT29 cells to oxaliplatin with gradual dose escalation. Relative to the parental HT29 cells, HT29/ox cells were 10 times as resistant to oxaliplatin (Table 1). Quantitative real-time reverse transcription polymerase chain reaction (RT-PCR) and Western blotting revealed that the HT29/ox cells showed up-regulated messenger RNA (mRNA) as well as protein for MTR and MT1Q compared with HT29 cells (Fig. 4, A and B). Moreover, the down-regulation of MT1Q and MTR with small interfering RNA (siRNA) restored the sensitivity of HT29/ox cells to oxaliplatin (fig. S6). In vitro cytotoxicity studies showed that DACHPt/m was 120 times as cytotoxic as oxaliplatin in HT29/ox cells (Table 1). These results suggested that DACHPt/m may overcome acquired resistance to oxaliplatin.

In vivo intratumoral imaging of F-DACHPt/m in a human colon cancer model

DACHPt/m would need to extravasate, penetrate into the interstitial tissue, and be internalized by cancer cells after systemic administration to exert the in vivo antitumor activity predicted from the results above. We performed real-time intravital observation of the accumulation and subcellular fate of F-DACHPt/m in HT29 xenografts by using in vivo CLSM equipped with a high-speed resonant scanner developed to acquire live tissue images of experimental animals (fig. S7). Immediately after intravenous injection, F-DACHPt/m was observed in the blood vessels of solid tumors (Fig. 5A and video S2). The fluorescence from F-DACHPt/m in the blood vessels corresponded only to that of BODIPY FL. Even 12 hours later, only BODIPY FL fluorescence was observed flowing in the blood vessels (Fig. 5B and video S3). These observations indicate that F-DACHPt/m stably circulates in the bloodstream while maintaining their micellar structure. Images of tumor tissue revealed the accumulation and dissociation behaviors of F-DACHPt/m (Fig. 5, C and D, and video S3). Two hours after injection, F-DACHPt/m accumulated within the tumor tissue because of the EPR effect and was identified within the cells, whereas BODIPY TR fluorescence remained quenched. BODIPY TR fluorescence gradually appeared inside the cells 4 hours after injection and was clearly visible after 12 hours, indicating the release of DACHPt

Table 1. In vitro cytotoxicity of free oxaliplatin and DACHPt/m against HT29 and HT29/ox cells after a 48-hour incubation. Data are expressed as means ± SEM (n = 4).

Cells	IC_{50} (μM)*		
	Free oxaliplatin	DACHPt/m	Oxaliplatin/DACHPt/m
HT29	2.2 ± 2.2	0.47 ± 0.05	4.7
HT29/ox	22.8 ± 2.6	0.19 ± 0.11	120
Ratio of HT29/ox/HT29	10.4	0.4	—

*IC_{50} values obtained from the MTT assay.

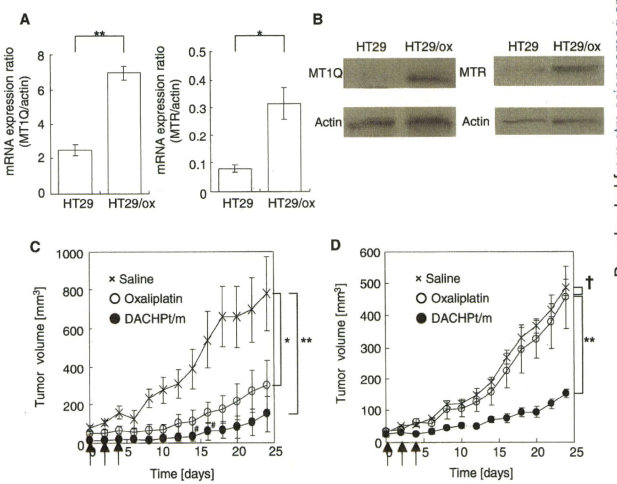

Fig. 4. Expression of MT1Q and MTR in HT29/ox cells and effects of DACHPt/m on HT29 and HT29/ox tumors in vivo. (**A**) Relative mRNA expression of metallothionein (MT1Q) and methionine synthase (MTR) in parent HT29 and HT29/ox cell lines. Data are expressed as means ± SEM (n = 3). *P < 0.05; **P < 0.01. (**B**) Western blots of MT1Q and MTR in HT29 and HT29/ox cell lines. (**C** and **D**) In vivo effect of DACHPt/m on subcutaneous HT29 (C) and HT29/ox (D) tumor cells. Crosses, saline; open circles, oxaliplatin (8 mg/kg); filled circles, DACHPt/m (4 mg/kg); arrows, injection of oxaliplatin and DACHPt/m; #, tumor regression; †P > 0.1; *P < 0.05; **P < 0.01. Data are expressed as means ± SEM (n = 4).

from the micelles inside the cells in the tumor tissue. The cell membrane, stained with CellMask, and cell nuclei were substantially free of F-DACHPt/m (Fig. 5, C and D, and video S3). These results were consistent with our in vitro results (Fig. 3A) and suggested that F-DACHPt/m percolated into interstitial tissues and was efficiently internalized to endosomal compartments of cells in a micelle form, followed by dissociation of the multimolecular structure of the micelles in the late endosomal and lysosomal compartments.

DACHPt/m enhances antitumor activity and overcomes oxaliplatin resistance in vivo

On the basis of our observations of the in vivo behavior of F-DACHPt/m, we hypothesized that DACHPt/m may also overcome oxaliplatin resistance in vivo. Thus, we evaluated DACHPt/m in vivo antitumor activity against subcutaneous HT29 and HT29/ox tumors (Fig. 4, C and D). Although free oxaliplatin failed to inhibit the growth of HT29/ox tumors, DACHPt/m exhibited substantial antitumor activity in the oxaliplatin-resistant xenograft model and successfully overcame the oxaliplatin resistance of HT29/ox cells in vivo (Fig. 4D). Note that DACHPt/m also achieved higher antitumor activity than oxaliplatin against the HT29 tumors (Fig. 4C). Thus, our micelle-based drug delivery vehicle was able to circumvent the detoxification mechanisms against platinum drugs in tumor cell cytoplasm through selective subcellular drug release and hence overcome acquired resistance.

DISCUSSION

Colorectal cancer is a major cause of morbidity and mortality worldwide (*1*). Oxaliplatin is currently the standard therapy for colorectal cancer, and acquired resistance to oxaliplatin is a major clinical drawback in the treatment of colorectal cancer [virtually all metastatic colorectal cancer becomes resistant to oxaliplatin, with a median time to progression of 8.7 months (*40*)]. The major cellular processes by which oxaliplatin enters and attacks cancer cells include uptake and transport, formation of DNA adducts and their recognition by damage response proteins, and signal transduction leading to apoptosis. Any factors that interfere with these pathways can lead to drug resistance (*41*). Here, we showed that DACHPt/m can overcome drug resistance by circumventing recognition by MTR and MT1Q, and achieve subcellular drug delivery both in vitro and in vivo to the perinuclear region of cells. It has been reported that drug delivery systems can overcome multidrug resistance

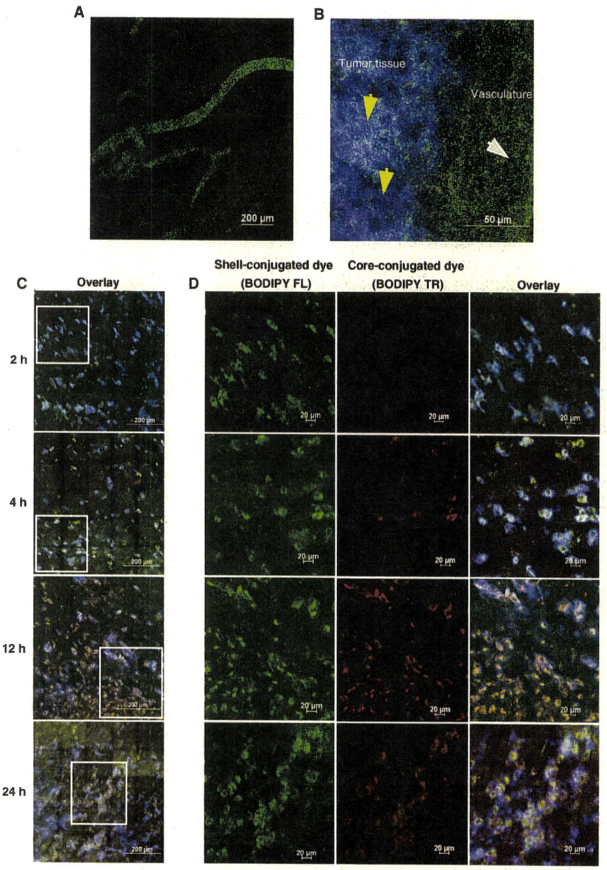

Fig. 5. In vivo CLSM observation of F-DACHPt/m in blood vessels and tumors after intravenous administration. (**A** and **B**) CLSM observation of F-DACHPt/m in the blood vessels of solid tumors (A) immediately after injection and (B) in the tumor tissue at 12 hours after injection. Yellow arrows, tumor tissue; white arrow, blood vessel. (**C**) Time-dependent CLSM observation of F-DACHPt/m in the tumor tissues at 2, 4, 12, and 24 hours after injection. Green, fluorescence from the shell-conjugated dyes (BODIPY FL); red, core-conjugated dyes (BODIPY TR); blue, cell surfaces stained by CellMask. (**D**) Magnification of selected areas [square regions in (C)] by channel.

by avoiding the drug efflux mechanism of P-glycoprotein (*20*–*22*). Because P-glycoprotein is not associated with platinum drug resistance (*42*), we used a different approach. Our data indicate that cytoplasmic detoxification mechanisms against platinum drugs can potentially be avoided by using the appropriate drug delivery system.

Nanocarriers encounter numerous barriers in vivo en route to their target during the processes of blood circulation, extravasation, penetration, and cellular uptake. It is therefore difficult to extrapolate in vivo outcomes of a drug-nanocarrier combination from its in vitro behavior, although real-time observation of in vivo behaviors such as we have used here can ascertain critical barriers residing in a living body and facilitate the design of a nanocarrier optimized for in vivo delivery. The in vivo CLSM technique that we used in this study enabled spatiotemporal and quantitative analyses of extravasation, tissue penetration, and cellular internalization of nanocarriers in living animals. Using dual fluorescent labeling of DACHPt/m, we elucidated the real-time intratumoral behavior of DACHPt/m. The dual fluorescent label of DACHPt micelles allowed us to trace the micelles' position by the ever-present fluorescent signal from the surface of the micelles, and the drug release and dissociation of the multimolecular structure of the micelles by the dequenching and fluorescence recovery of the core-conjugated dye. In in vitro cellular experiments, these micelles were internalized intact, and then they were disassembled and the drug was released in late endosomes. In our in vivo microscopy, we observed that DACHPt/m maintained their micelle form during circulation in the blood, probably because of the stable inner core structure formed by the polymer-metal complexes, and extravasated into solid tumors. DACHPt/m was able to deeply penetrate cancerous tissue after extravasation and was internalized by different cell populations that were distant from the blood vessels. Such efficient penetration of tissue is a requirement of successful drug delivery and a prerequisite for effective subcellular targeting. It has been reported that PEG-modified liposomes with 100-nm diameter accumulated at perivascular regions of solid tumors and failed to penetrate the tumor interstitium deeply (*43*). Although this characteristic may depend on the cancer type, it is possible that the deep tumor penetration of DACHPt/m is a result of their smaller 30-nm size. Finally, the DACHPt/m structure dissociated at the perinuclear regions of the cell after internalization, based on the pH and chloride ion concentration–selective release of DACHPt. This observation is also consistent with our hypothesis that DACHPt/m can overcome oxaliplatin resistance in tumors by bypassing the cytoplasmic detoxification mechanisms of MTR and MT1Q. There are, however, several limitations to the type of study that we have performed in a subcutaneous tumor model. Compared with subcutaneous tumors, orthotopic and spontaneously forming tumors may have characteristic differences such as vascular density and degree of fibrosis, which may affect the transport of nanocarriers (*44*).

Our research provides one approach for subcellular targeting of cytoplasmic drugs. Such nanocarriers have the potential to enhance the drug efficacy and overcome drug resistance.

MATERIALS AND METHODS

Materials

γ-Benzyl L-glutamate and bis(trichloromethyl) carbonate (triphosgene) were purchased from Sigma Chemical and Tokyo Kasei Kogyo, respectively. *N*,*N*-Dimethylformamide (DMF), 3-(4,5-dimethylthiazol-2-yl)-2,5-diphenyltetrazolium bromide (MTT), and dimethyl sulfoxide (DMSO) were purchased from Wako Pure Chemicals. Oxaliplatin and $NaCH_3CN$ were purchased from Sigma-Aldrich Inc. Dichloro(1,2-diammino cyclohexane) platinum(II) was purchased from W. C. Heraeus GmbH. α-Methoxy-ω-amino-poly(ethylene glycol) [CH_3O-PEG-NH_2; molecular weight (MW), 12,000] was purchased from Nippon Oil and Fats. BODIPY TR-succinimidyl ester, BODIPY FL-hydrazide, LysoTracker Blue, CellLight Early Endosome-RFP (Rab5a-RFP), CellMask, and Lipofectamine RNAiMAX were purchased from Invitrogen.

Cell lines and animals

HT29 cells were purchased from the American Type Culture Collection. HT29 cells were maintained in McCoy's 5A modified medium (Invitrogen) containing 10% fetal bovine serum (Gibco) as well as 1% penicillin and streptomycin (Sigma) and were cultured at 37°C in a humidified atmosphere of 5% CO_2. To develop HT29/ox cells (*45*), we treated HT29 cells with oxaliplatin at IC_{50} doses for 1 hour. After 24 hours, cells were subcultured into new flasks and oxaliplatin was added to a culture of 80% confluent cells. The concentration was incrementally increased by factors of 1.2 to 2. The process was continued until the cells were resistant to drug concentrations at least 10 times as great. BALB/c-nu/nu mice (female; body weight, 18 to 20 g; age, 6 weeks old) were purchased from Charles River Japan. All animal experiments were carried out in accordance with the guidelines for animal experiments at the University of Tokyo, Japan.

Methods

Synthesis of block copolymers. α-4-(Diethoxymethyl)benzyl-ω-amino-poly(ethylene glycol) (Ac-Bz-PEG-NH_2) was previously synthesized in our laboratory (*46*). Poly(ethylene glycol)-*b*-poly(L-glutamic acid) [PEG-*b*-P(Glu)] [MW_{PEG}, 12,000; polymerization degree of P(Glu), 20] and Ac-Bz-PEG-*b*-poly(L-glutamic acid) [Ac-Bz-PEG-*b*-P(Glu)] [MW_{PEG}, 12,000; polymerization degree of P(Glu), 20] were synthesized according to the previously described synthetic method (*47*). Briefly, *N*-carboxyanhydride of γ-benzyl L-glutamate (BLG-NCA) was synthesized by the Fuchs-Farthing method with triphosgene (*48*). BLG-NCA was polymerized in DMF initiated by the amino group of CH_3O-PEG-NH_2 or Ac-Bz-PEG-NH_2 to obtain PEG-*b*-poly(γ-benzyl L-glutamate) (PEG-*b*-PBLG) or Ac-Bz-PEG-*b*-PBLG, respectively. The MW distribution of PEG-*b*-PBLG and Ac-Bz-PEG-*b*-PBLG was determined by gel permeation chromatography (GPC) [column, TSK-gel G3000HHR, G4000HHR (Tosoh); eluent, DMF containing 10 mM LiCl; flow rate, 0.8 ml/min; detector, refractive index; temperature, 25°C]. PEG-*b*-PBLG and Ac-Bz-PEG-*b*-PBLG showed narrow MW distributions (M_w/M_n: 1.09 and 1.16, respectively) in GPC. The degrees of polymerization of PBLG in PEG-*b*-PBLG and Ac-Bz-PEG-*b*-PBLG were determined to be 20 by comparing the proton ratios of methylene units in PEG (-OCH_2CH_2-: δ = 3.7 ppm) and phenyl groups of PBLG (-$CH_2C_6H_5$: δ = 7.3 ppm) in ^{1}H-NMR (nuclear magnetic resonance) measurement. Both PEG-*b*-PBLG and Ac-Bz-PEG-*b*-PBLG were deprotected by mixing with 0.5 N NaOH at room temperature to obtain PEG-*b*-P(Glu) and Ac-Bz-PEG-*b*-P(Glu), respectively. Complete deprotection was confirmed by ^{1}H NMR measurement.

Preparation of micelles. For conjugation of BODIPY TR to a polymer, a solution of BODIPY TR-succinimidyl ester in DMSO (1 mg/ml) was mixed with Ac-Bz-PEG-*b*-P(Glu). The reaction was carried out overnight at room temperature with stirring. Unreacted

BODIPY TR was removed by dialysis [MW cutoff (MWCO) size, 2000 daltons] against DMSO and water. To conjugate BODIPY FL to the Ac-Bz-PEG-*b*-P(Glu)-BODIPY TR polymer, we mixed a solution of BODIPY FL-hydrazide in DMSO with the polymer, followed by the addition of 1 N HCl to deprotect the acetal group. Samples were stirred overnight at room temperature and treated with $NaBH_3CN$ to reduce the link between BODIPY FL and the polymer. For purification, unbound BODIPY FL was removed by dialysis (MWCO, 2000 daltons) against DMSO and water. The prepared BODIPY FL-PEG-*b*-P(Glu)-BODIPY TR copolymer was freeze-dried overnight and stored at −20°C. DACHPt/m and F-DACHPt/m were prepared according to the previously described method (*23*). DACHPt (5 mM) was suspended in distilled water and mixed with silver nitrate ([$AgNO_3$]/[DACHPt] = 1) to form aqueous complexes. The solution was kept in the dark at 25°C for 24 hours. AgCl precipitates were eliminated by centrifugation. The supernatant was purified by passage through a 0.22-μm filter. DACHPt aqueous complex solution was then mixed with PEG-*b*-P(Glu) or BODIPY FL-PEG-*b*-P(Glu)-BODIPY TR ([Glu] = 5 mM; [DACHPt]/[Glu] = 1.0) and reacted for 120 hours to obtain DACHPt/m or F-DACHPt/m, respectively. DACHPt/m and F-DACHPt/m were purified by ultrafiltration (MWCO, 30,000 daltons; Fig. 1A). The size distributions of DACHPt/m and F-DACHPt/m were evaluated by dynamic light scattering at 25°C with a Zetasizer Nano ZS90 (Malvern Instruments). The platinum content of DACHPt/m was determined by ion-coupled plasma mass spectrometry (4500 ICP-MS; Hewlett Packard).

Drug release and fluorescence profiles of micelles under different conditions. The release of platinum from DACHPt/m and F-DACHPt/m in phosphate-buffered saline (PBS) at 37°C was evaluated as described (*23*). Briefly, a micelle solution of known platinum concentration was placed inside a dialysis bag (MWCO, 2000 daltons). The solution was then dialyzed against PBS under different conditions mimicking the extracellular environment (10 mM PBS, pH 7.4, and 150 mM NaCl), early endosomes (10 mM PBS, pH 6.9, and 20 mM NaCl), and late endosomes (10 mM PBS, pH 5.5, and 70 mM NaCl) at 37°C (*25*). The concentration of platinum present in the dialysate was determined with ICP-MS. The fluorescence profiles of F-DACHPt/m were also evaluated under the same conditions with a spectrofluorometer (FP6600, Jasco) or NanoDrop (ND3300, Scrum). Changes in fluorescence intensity were measured at a defined time period.

In vitro observation of subcellular localization and the fate of F-DACHPt/m by CLSM. HT29 cells were cultured at 1×10^5 cells in 35-mm glass-based dishes (Asahi Techno Glass). After overnight incubation in a fresh medium, the cells were washed twice with PBS. The medium was then replaced by 1 ml of fresh medium containing F-DACHPt/m (100 μM on Pt base). Live-cell CLSM imaging was performed with a Zeiss LSM 510 META nonlinear optics scan head attached to an inverted Axiovert 200 M SP equipped with a 63 × 1.4 numerical aperture Plan Apochromat oil immersion objective (Carl Zeiss). For long-term time-lapse imaging, culture dishes were wrapped with an optically clear foil cover (Carl Zeiss) to avoid evaporation and mounted onto the microscope stage incubator (37°C, 5% CO_2, 90% relative humidity). Bright-field DIC (differential interference contrast) images and fluorescent sequences were taken every 30 min for 72 hours. BODIPY FL was excited at 488 nm with an Ar laser and fluorescence was detected at 500 to 530 nm, whereas BODIPY TR was excited at 543 nm with a He-Ne laser, and fluorescence was detected at 565 to 615 nm. Laser power was kept low at 0.36 mW for 488 nm and at 0.018 mW for 543 nm so that photobleaching was negligible. To determine whether DACHPt/m was taken up by endocytosis, we treated HT29 cells with F-DACHPt/m at 37°C or 4°C for 6 hours and then observed by CLSM. For the colocalization studies, we used micelles prepared from BODIPY FL-PEG-P(Glu) that only emit fluorescence from the shell. HT29 cells, which had been preincubated with CellLight Early Endosome-RFP to express an early endosome marker, Rab5a-RFP, were treated with BODIPY FL–conjugated DACHPt/m, and images were taken at indicated time points after staining with LysoTracker Blue. Rab5a-RFP was excited at 543 nm with a He-Ne laser, and fluorescence was detected at 565 to 615 nm. LysoTracker Blue was excited in multiphoton mode at 710 nm with a Mai Tai tunable broadband laser (Spectra-Physics), and fluorescence was detected at 390 to 465 nm. Colocalization was quantified as follows:

$$\text{amount of colocalization (\%)} = \text{BODIPY FL pixels}_{\text{colocalization}}/\text{BODIPY FL pixels}_{\text{total}} \times 100$$

where BODIPY FL $\text{pixels}_{\text{colocalization}}$ represents the number of BODIPY FL pixels colocalizing with Rab5a-RFP or LysoTracker pixels in the cytoplasm, and BODIPY FL $\text{pixels}_{\text{total}}$ represents the number of all BODIPY FL pixels in the cytoplasm. The timing and location of the micelle dissociation and concomitant drug release were studied by evaluating the colocalization of BODIPY FL and BODIPY TR signals from F-DACHPt/m with the late endosomes/lysosomes (Fig. 3, E and F). Cells were treated with F-DACHPt/m, and images were taken at indicated time points after staining with LysoTracker Blue. Colocalization was quantified as follows:

$$\text{amount of colocalization (\%)} = \text{BODIPY FL or BODIPY TR pixels}_{\text{colocalization}}/\text{BODIPY FL or BODIPY TR pixels}_{\text{total}} \times 100$$

where BODIPY FL or BODIPY TR $\text{pixels}_{\text{colocalization}}$ represents the number of BODIPY FL or BODIPY TR pixels colocalizing with LysoTracker pixels in the cytoplasm, and BODIPY FL or BODIPY TR $\text{pixels}_{\text{total}}$ represents the number of all BODIPY FL or BODIPY TR pixels in the cytoplasm.

Determination of subcellular Pt accumulation and amount of Pt-DNA adducts. HT29 cells (6×10^6) were seeded in 100-mm tissue culture dishes. After 24 hours, cells were treated with 10 μM oxaliplatin or DACHPt/m on a platinum base. After 6, 8, 12, and 24 hours of drug exposure, the medium was removed and the cells were washed three times with PBS, scraped, and harvested. Samples were freeze-dried overnight, dissolved in heated nitric acid, and evaporated to dryness. The samples were redissolved in water and the Pt content was determined by ICP-MS. For the quantification of Pt-DNA adducts, DNA was extracted with a DNA purification kit (Promega) according to the manufacturer's protocol. The amount and purity of DNA were determined by measuring absorption at 260 and 280 nm with NanoDrop (ND3300). The DNA was dissolved in nitric acid, dried, and redissolved in water. The Pt content was determined by ICP-MS, and the DNA platination levels were expressed as micrograms of Pt per milligram of DNA.

In vitro cytotoxicity study against human cancer cells. The in vitro cytotoxicity of oxaliplatin and DACHPt/m was examined against a panel of 37 human cancer cells as described (*34*, *35*). Cancer cells were plated into flat-bottomed 96-well plates at 5×10^3 per well. Cells were treated by continuous exposure to oxaliplatin or DACHPt/m in a final volume of 100 μl. Plates were incubated for 48 hours at 37°C in a humidified atmosphere with 5% CO_2, and cell viability was determined

by MTT assay. To determine the relationship between cellular sensitivity to oxaliplatin or DACHPt/m and the expression of genes involved in the sensitivity or resistance of cells to platinum compounds, we assessed the gene expression profile of 21 human cancer cell lines for 26 genes selected on the basis of previous studies on cisplatin- or oxaliplatin-resistant cells (*36*). Expression of these individual genes was determined by searching the National Cancer Institute database. The coefficient of correlation between the GI_{50}s of free oxaliplatin and DACHPt/m as well as the level of gene expression was calculated for each gene.

Quantitative real-time RT-PCR. The expression of the metallothionein (MT1Q) [human MT1B (same as MT1Q), NM_005947, 4MQ-012725-01-0002] and methionine synthase (MTR) (human MTR, NM_000254, 4LQ-009896-00-0002) was confirmed by quantitative real-time RT-PCR. After 24 hours of treatment, cells were washed with PBS and harvested. Total RNA was prepared with TRIzol (Invitrogen), and complementary DNA (cDNA) was reverse-transcribed with a QuantiTect reverse transcription kit (Qiagen). PCR primer sequences were as follows: MT1Q, 5′-GAACTCCAGGCTTGTCTTGG-3′ (forward) and 5′-CATTTGCACTCTTTGCACTTG-3′ (reverse); MTR, 5′-ACCCAACTTCCAGGGAGACT-3′ (forward) and 5′-GGCAC-CATGATCTTGGACTT-3′ (reverse); actin, 5′-AGATGTGGATCAG-CAAGCAG-3′ (forward) and 5′-GCGCAAGTTAGGTTTTGTCA-3′ (reverse); and 18S, 5′-CGGCGACGACCCATTCGAAC-3′ (forward) and 5′-GAATCGAACCCTGATTCCCCGTC-3′ (reverse). cDNA from HT29 cells was amplified with specific primers with a SYBR Green Core Reagent Kit (Qiagen) and a real-time PCR instrument (Applied Biosystems). Expression of each gene was standardized with endogenous actin or 18S as a control, and its relative levels in HT29 or HT29/ox cells were quantified by calculating $2^{-\Delta\Delta C_T}$, where $\Delta\Delta C_T$ is the difference in C_T (cycle number at which the amount of amplified target reaches a fixed threshold) between target and reference.

MT1Q and MTR gene knockdown. The siRNAs against MT1Q and MTR and the control siRNA were purchased from Thermo Fisher Scientific Inc. The siRNA target sequences against MT1Q are the following: siMT1Q, GCAAAGGCUCAUCAGAGAA. The siRNA sequences against MTR are the following: siMTR, CUGAGAAGCU-CUUACGUUA. The siRNAs were transfected into the cell with Lipofectamine RNAiMAX (Invitrogen) according to the instructions of the manufacturer. Briefly, HT29/ox cells (4×10^5) were seeded in six-well plates. Twenty-four hours later, the mixture of siMT1Q (50 nM) and siMTR (50 nM) was transfected into the cells with Lipofectamine RNAiMAX reagent. Knockdown of MT1Q and MTR was separately confirmed by real-time PCR (fig. S6, A and B, respectively). To investigate the role of MT1Q and MTR in the oxaliplatin resistance in HT29/ox cells, we seeded HT29/ox cells (5×10^3) in 96-well plates, and 24 hours later, the mixture of siMT1Q (50 nM) and siMTR (50 nM) or the control siRNA was transfected into the cells with Lipofectamine RNAiMAX reagent. Twenty-four hours after transfection, the transfected HT29/ox cells were treated by continuous exposure to oxaliplatin in a final volume of 100 μl. Plates were further incubated for 48 hours at 37°C in a humidified atmosphere with 5% CO_2, and their cytotoxicity was determined by MTT assay.

Western blotting. HT29 or HT29/ox cells (5×10^6) were seeded in 100-mm^2 plates and washed with PBS (100 μl). Cell extracts were resolved in TNE buffer [1% NP-40, 150 mM NaCl, 10 mM tris-HCl, 1 mM EDTA, aprotinin (10 μg/ml), 2 mM Na_3VO_4, 10 mM NaF]. The cell suspension was centrifuged for 20 min at 15,000*g*. Sampling buffer (4×) was added to the aliquots, followed by incubation for 5 min at 100°C. Transfer to a polyvinylidene difluoride membrane (Invitrogen) was performed by electrophoresis for 90 min at 125 V. Membranes were blocked with 6% nonfat milk or tris-buffered saline (TBS) with 0.1% Tween 20 (MT1Q) for 1 hour. They were then probed at room temperature with the following antibodies: anti-metallothionein (ab12228, 1:1000, Abcam), anti–methionine synthase (ab66039, 1:2000, Abcam), and anti–β-actin (#4967, 1:1000, Cell Signaling). Membranes were washed three times with washing buffer (TBS with 0.1% Tween 20) and then probed with the secondary anti–rabbit immunoglobulin G (IgG) horseradish peroxidase (HRP) (W401B, 1:10,000, Promega) or anti–mouse IgG HRP (W402B, 1:10,000, Promega) conjugate for 1 hour. The secondary antibody was washed three times with washing buffer and then evenly coated with enhanced chemiluminescence (ECL) Western blotting detection reagents (GE Healthcare) for 30 s. The membrane was immediately exposed to Fuji Medical X-ray film (Fujifilm) at room temperature for various periods in a film cassette. Protein levels were standardized with the signal from the β-actin probe.

In vivo antitumor activity studies. BALB/c-nu/nu mice (female, $n = 4$) were inoculated subcutaneously with HT29 or HT29/ox cells (1×10^7/ml). Tumors were allowed to grow for 1 week (tumor size at this point was about 40 mm^3). Mice were then treated intravenously three times at 2-day intervals with oxaliplatin (8 mg/kg) or DACHPt/m (4 mg/kg) on a platinum base. Antitumor activity was evaluated in terms of tumor size (V) with the following equation:

$$V = a \times b^2/2$$

Here, a and b are the major and minor axes, respectively, of the tumor as measured by a caliper.

Intravital observation of the in vivo behavior of F-DACHPt/m. Intravital observation of F-DACHPt/m was performed as described (*49*). Female BALB/c mice (6 to 8 weeks old) were inoculated subcutaneously with HT29 cells (1×10^7/ml). After 5 days, when the tumor volumes reached 70 mm^3, F-DACHPt/m (10 mg/kg) was administered intravenously. At 2, 4, 12, and 24 hours after treatment, mice were anesthetized with 2.5% isoflurane (Abbott Japan) with a Univentor 400 Anesthesia Unit (Univentor). An arc-shaped incision was made around the subcutaneous tumor, and the skin flap was elevated without injuring the feeding vessels. The mouse was placed directly onto a thermoplate (Tokai Hit), and the skin flap was everted and stretched with several bent 30-gauge needles. The plasma membrane stain, CellMask Deep Red, was directly applied to the subcutaneous tumor, and a coverslip (Muto Pure Chemicals) was attached with just enough pressure to flatten the tumor surface. All in vivo images were acquired with a Nikon A1R CLSM attached to an upright Eclipse FN1 (Nikon). The A1R incorporates a conventional galvano scanner and a high-speed resonant scanner. The latter allows an acquisition speed of 30 frames per second while maintaining a relatively high resolution of 512 × 512 scanned points. BODIPY FL, BODIPY TR, and CellMask were excited with three lasers (488-nm Ar, 560-nm He-Ne, and 640-nm He-Ne lasers), and the fluorescent signals were detected. Laser powers were kept at 19.5 mW for 488-nm Ar, 7.5 mW for 561-nm He-Ne, and 1 mW for 640-nm He-Ne.

Statistical analysis. Data are presented as means ± SEM. The significant differences between the groups were analyzed by a Student's t test, and a P value of <0.05 was considered significant.

SUPPLEMENTARY MATERIAL

www.sciencetranslationalmedicine.org/cgi/content/full/3/64/64ra2/DC1

Fig. S1. Synthetic scheme of BODIPY FL-PEG-*b*-P(Glu)-BODIPY TR.

Fig. S2. Size distribution of DACHPt/m and F-DACHPt/m as determined by dynamic light scattering.

Fig. S3. Fluorescent images of HT29 cells after 6-hour incubation with F-DACHPt/m at 37°C and 4°C.

Fig. S4. In vitro CLSM observation of dissociation of F-DACHPt/m in the late endosomes/lysosomes.

Fig. S5. In vitro cytotoxicity of oxaliplatin and DACHPt/m against a human cancer cell panel.

Fig. S6. Knockdown of MT1Q and MTR restores the sensitivity of HT29/ox to oxaliplatin.

Fig. S7. Schematic illustration of experimental settings of in vivo CLSM.

Table S1. Coefficient of correlation between the GI_{50}s of free oxaliplatin or DACHPt/m and the expression levels of genes involved in the sensitivity or resistance of cells to platinum compounds.

Video S1. In vitro live imaging.

Video S2. In vivo live imaging (immediately after injection).

Video S3. In vivo live imaging (12 hours after injection).

REFERENCES AND NOTES

1. A. Jemal, R. Siegel, E. Ward, Y. Hao, J. Xu, M. J. Thun, Cancer statistics, 2009. *CA Cancer J. Clin.* **59**, 225–249 (2009).
2. T. M. Allen, P. R. Cullis, Drug delivery systems: Entering the mainstream. *Science* **303**, 1818–1822 (2004).
3. M. Ferrari, Cancer nanotechnology: Opportunities and challenges. *Nat. Rev. Cancer* **5**, 161–171 (2005).
4. V. P. Torchilin, Recent advances with liposomes as pharmaceutical carriers. *Nat. Rev. Drug Discov.* **4**, 145–160 (2005).
5. R. Duncan, The dawning era of polymer therapeutics. *Nat. Rev. Drug Discov.* **2**, 347–360 (2003).
6. Y. Matsumura, H. Maeda, A new concept for macromolecular therapeutics in cancer chemotherapy: Mechanism of tumoritropic accumulation of proteins and the antitumor agent Smancs. *Cancer Res.* **46**, 6387–6392 (1986).
7. M. E. Davis, Z. G. Chen, D. M. Shin, Nanoparticle therapeutics: An emerging treatment modality for cancer. *Nat. Rev. Drug Discov.* **7**, 771–782 (2008).
8. N. Nishiyama, K. Kataoka, Current state, achievements, and future prospects of polymeric micelles as nanocarriers for drug and gene delivery. *Pharmacol. Ther.* **112**, 630–648 (2006).
9. M. Yokoyama, M. Miyauchi, N. Yamada, T. Okano, Y. Sakurai, K. Kataoka, S. Inoue, Characterization and anticancer activity of the micelle-forming polymeric anticancer drug adriamycin-conjugated poly(ethylene glycol)-poly(aspartic acid) block copolymer. *Cancer Res.* **50**, 1693–1700 (1990).
10. K. Kataoka, G. S. Kwon, M. Yokoyama, T. Okano, Y. Sakurai, Block copolymer micelles as vehicles for drug delivery. *J. Control. Release* **24**, 119–132 (1993).
11. K. Kataoka, A. Harada, Y. Nagasaki, Block copolymer micelles for drug delivery: Design, characterization and biological significance. *Adv. Drug Deliv. Rev.* **47**, 113–131 (2001).
12. A. V. Kabanov, E. V. Batrakova, D. W. Miller, Pluronic block copolymers as modulators of drug efflux transporter activity in the blood–brain barrier. *Adv. Drug Deliv. Rev.* **55**, 151–164 (2003).
13. Y. Matsumura, K. Kataoka, Preclinical and clinical studies of anticancer agent-incorporating polymer micelles. *Cancer Sci.* **100**, 572–579 (2009).
14. Y. Matsumura, T. Hamaguchi, T. Ura, K. Muro, Y. Yamada, Y. Shimada, K. Shirao, T. Okusaka, H. Ueno, M. Ikeda, N. Watanabe, Phase I clinical trial and pharmacokinetic evaluation of NK911, a micelle-encapsulated doxorubicin. *Br. J. Cancer* **91**, 1775–1781 (2004).
15. T. Hamaguchi, K. Kato, H. Yasui, C. Morizane, M. Ikeda, H. Ueno, K. Muro, Y. Yamada, T. Okusaka, K. Shirao, Y. Shimada, H. Nakahama, Y. Matsumura, A phase I and pharmacokinetic study of NK105, a paclitaxel-incorporating micellar nanoparticle formulation. *Br. J. Cancer* **97**, 170–176 (2007).
16. T. Hamaguchi, T. Doi, T. Eguchi-Nakajima, K. Kato, Y. Yamada, Y. Shimada, N. Fuse, A. Ohtsu, S. Matsumoto, M. Takanashi, Y. Matsumura, Phase I study of NK012, a novel SN-38–incorporating micellar nanoparticle, in adult patients with solid tumors. *Clin. Cancer Res.* **16**, 5058–5066 (2010).
17. R. H. Wilson, R. Plummer, J. Adam, M. M. Eatock, A. V. Boddy, M. Griffin, R. Miller, Y. Matsumura, T. Shimizu, H. Calvert, Phase I and pharmacokinetic study of NC-6004, a new platinum entity of cisplatin-conjugated polymer forming micelles. *J. Clin. Oncol.* **26**, 2573 (2008).
18. R. Dent, M. Trudeau, K. I. Pritchard, W. M. Hanna, H. K. Kahn, C. A. Sawka, L. A. Lickley, E. Rawlinson, P. Sun, S. A. Narod, Triple-negative breast cancer: Clinical features and patterns of recurrence. *Clin. Cancer Res.* **13**, 4429–4434 (2007).
19. J. A. Hubbell, Materials science. Enhancing drug function. *Science* **300**, 595–596 (2003).
20. T. Minko, P. Kopecková, J. Kopecek, Efficacy of the chemotherapeutic action of HPMA copolymer-bound doxorubicin in a solid tumor model of ovarian carcinoma. *Int. J. Cancer* **86**, 108–117 (2000).
21. D. Kim, E. S. Lee, K. T. Oh, Z. G. Gao, Y. H. Bae, Doxorubicin-loaded polymeric micelle overcomes multidrug resistance of cancer by double-targeting folate receptor and early endosomal pH. *Small* **4**, 2043–2050 (2008).
22. K. Cho, X. Wang, S. Nie, Z. G. Chen, D. M. Shin, Therapeutic nanoparticles for drug delivery in cancer. *Clin. Cancer Res.* **14**, 1310–1316 (2008).
23. H. Cabral, N. Nishiyama, S. Okazaki, H. Koyama, K. Kataoka, Preparation and biological properties of dichloro(1,2-diaminocyclohexane)platinum(II) (DACHPt)-loaded polymeric micelles. *J. Control. Release* **101**, 223–232 (2005).
24. H. Cabral, N. Nishiyama, K. Kataoka, Optimization of (1,2-diamino-cyclohexane)platinum(II)-loaded polymeric micelles directed to improved tumor targeting and enhanced antitumor activity. *J. Control. Release* **121**, 146–155 (2007).
25. N. D. Sonawane, J. R. Thiagarajah, A. S. Verkman, Chloride concentration in endosomes measured using a ratioable fluorescent Cl^- indicator: Evidence for chloride accumulation during acidification. *J. Biol. Chem.* **277**, 5506–5513 (2002).
26. N. Nishiyama, F. Koizumi, S. Okazaki, Y. Matsumura, K. Nishio, K. Kataoka, Differential gene expression profile between PC-14 cells treated with free cisplatin and cisplatin-incorporated polymeric micelles. *Bioconjug. Chem.* **14**, 449–457 (2003).
27. I. D. Johnson, H. C. Kang, R. P. Haugland, Fluorescent membrane probes incorporating dipyrrometheneboron difluoride fluorophores. *Anal. Biochem.* **198**, 228–237 (1991).
28. S. Arnould, I. Hennebelle, P. Canal, R. Bugat, S. Guichard, Cellular determinants of oxaliplatin sensitivity in colon cancer cell lines. *Eur. J. Cancer* **39**, 112–119 (2003).
29. L. Kelland, The resurgence of platinum-based cancer chemotherapy. *Nat. Rev. Cancer* **7**, 573–584 (2007).
30. E. Raymond, S. Faivre, S. Chaney, J. Woynarowski, E. Cvitkovic, Cellular and molecular pharmacology of oxaliplatin. *Mol. Cancer Ther.* **1**, 227–235 (2002).
31. F. R. Luo, T. Y. Yen, S. D. Wyrick, S. G. Chaney, High-performance liquid chromatographic separation of the biotransformation products of oxaliplatin. *J. Chromatogr. B Biomed. Sci. Appl.* **724**, 345–356 (1999).
32. F. R. Luo, S. D. Wyrick, S. G. Chaney, Biotransformations of oxaliplatin in rat blood in vitro. *J. Biochem. Mol. Toxicol.* **13**, 159–169 (1999).
33. R. Duncan, Polymer conjugates as anticancer nanomedicines. *Nat. Rev. Cancer* **6**, 688–701 (2006).
34. T. Yamori, A. Matsunaga, S. Sato, K. Yamazaki, A. Komi, K. Ishizu, I. Mita, H. Edatsugi, Y. Matsuba, K. Takezawa, O. Nakanishi, H. Kohno, Y. Nakajima, H. Komatsu, T. Andoh, T. Tsuruo, Potent antitumor activity of MS-247, a novel DNA minor groove binder, evaluated by an *in vitro* and *in vivo* human cancer cell line panel. *Cancer Res.* **59**, 4042–4049 (1999).
35. S. Yaguchi, Y. Fukui, I. Koshimizu, H. Yoshimi, T. Matsuno, H. Gouda, S. Hirono, K. Yamazaki, T. Yamori, Antitumor activity of ZSTK474, a new phosphatidylinositol 3-kinase inhibitor. *J. Natl. Cancer Inst.* **98**, 545–556 (2006).
36. A. Vekris, D. Meynard, M. C. Haaz, M. Bayssas, J. Bonnet, J. Robert, Molecular determinants of the cytotoxicity of platinum compounds: The contribution of *in silico* research. *Cancer Res.* **64**, 356–362 (2004).
37. S. L. Kelley, A. Basu, B. A. Teicher, M. P. Hacker, D. H. Hamer, J. S. Lazo, Overexpression of metallothionein confers resistance to anticancer drugs. *Science* **241**, 1813–1815 (1988).
38. J. Holford, P. J. Beale, F. E. Boxall, S. Y. Sharp, L. R. Kelland, Mechanisms of drug resistance to the platinum complex ZD0473 in ovarian cancer cell lines. *Eur. J. Cancer* **36**, 1984–1990 (2000).
39. P. M. Deegan, I. S. Pratt, M. P. Ryan, The nephrotoxicity, cytotoxicity and renal handling of a cisplatin-methionine complex in male Wistar rats. *Toxicology* **89**, 1–14 (1994).
40. R. M. Goldberg, D. J. Sargent, R. F. Morton, C. S. Fuchs, R. K. Ramanathan, S. K. Williamson, B. P. Findlay, H. C. Pitot, S. R. Alberts, A randomized controlled trial of fluorouracil plus leucovorin, irinotecan, and oxaliplatin combinations in patients with previously untreated metastatic colorectal cancer. *J. Clin. Oncol.* **22**, 23–30 (2004).
41. D. Wang, S. J. Lippard, Cellular processing of platinum anticancer drugs. *Nat. Rev. Drug Discov.* **4**, 307–320 (2005).
42. I. Pastan, M. M. Gottesman, K. Ueda, E. Lovelace, A. V. Rutherford, M. C. Willingham, A retrovirus carrying an *MDR1* cDNA confers multidrug resistance and polarized expression of P-glycoprotein in MDCK cells. *Proc. Natl. Acad. Sci. U.S.A.* **85**, 4486–4490 (1988).
43. R. K. Jain, Delivery of molecular and cellular medicine to solid tumors. *Adv. Drug Deliv. Rev.* **46**, 149–168 (2001).
44. Y. Saito, M. Yasunaga, J. Kuroda, Y. Koga, Y. Matsumura, Antitumour activity of NK012, SN-38-incorporating polymeric micelles, in hypovascular orthotopic pancreatic tumour. *Eur. J. Cancer* **46**, 650–658 (2010).
45. M. Mishima, G. Samimi, A. Kondo, X. Lin, S. B. Howell, The cellular pharmacology of oxaliplatin resistance. *Eur. J. Cancer* **38**, 1405–1412 (2002).

46. Y. Akiyama, Y. Nagasaki, K. Kataoka, Synthesis of heterotelechelic poly(ethylene glycol) derivatives having α-benzaldehyde and ω-pyridyl disulfide groups by ring opening polymerization of ethylene oxide using 4-(diethoxymethyl)benzyl alkoxide as a novel initiator. *Bioconjug. Chem.* **15**, 424–427 (2004).
47. N. Nishiyama, S. Okazaki, H. Cabral, M. Miyamoto, Y. Kato, Y. Sugiyama, K. Nishio, Y. Matsumura, K. Kataoka, Novel cisplatin-incorporated polymeric micelles can eradicate solid tumors in mice. *Cancer Res.* **63**, 8977–8983 (2003).
48. W. H. Daly, D. Poche, The preparation of N-carboxyanhydrides of α-amino acids using bis(trichloromethyl)carbonate. *Tetrahedron Lett.* **29**, 5859–5862 (1988).
49. Y. Matsumoto, T. Nomoto, H. Cabral, Y. Matsumoto, S. Watanabe, R. J. Christie, K. Miyata, M. Oba, T. Ogura, Y. Yamasaki, N. Nishiyama, T. Yamasoba, K. Kataoka, Direct and instantaneous observation of intravenously injected substances using intravital confocal micro-videography. *Biomed. Opt. Express* **1**, 1209–1216 (2010).
50. **Acknowledgments:** M.M. thanks J. Ghaugas for his support and suggestions for preparing the manuscript and S. Hiro for his help with in silico data analysis. **Funding:** This research was supported in part by Funding Program for World-Leading Innovative R&D on Science and Technology (FIRST Program) from the Japan Society for the Promotion of Science (JSPS) and the Core Research Program for Evolutional Science and Technology (CREST) from the Japan Science and Technology Agency (JST). **Author contributions:** M.M. and H.C. designed and performed the experiments, analyzed the results, and wrote the manuscript. Y.M. performed the imaging experiments. S.W. performed the siRNA knockdown studies. T.Y. conducted human cell panel analysis. M.R.K. edited the manuscript. N.N. supervised the project and wrote the manuscript. K.K. supervised the project and edited the manuscript. **Competing interests:** The authors declare that they have no competing interests.

Submitted 14 June 2010
Accepted 10 December 2010
Published 5 January 2011
10.1126/scitranslmed.3001385

Citation: M. Murakami, H. Cabral, Y. Matsumoto, S. Wu, M. R. Kano, T. Yamori, N. Nishiyama, K. Kataoka, Improving drug potency and efficacy by nanocarrier-mediated subcellular targeting. *Sci. Transl. Med.* **3**, 64ra2 (2011).

Biomaterials 32 (2011) 652–663

Contents lists available at ScienceDirect

Biomaterials

journal homepage: www.elsevier.com/locate/biomaterials

Polyplex micelles prepared from ω-cholesteryl PEG-polycation block copolymers for systemic gene delivery

Makoto Oba [a], Kanjiro Miyata [b], Kensuke Osada [c], R. James Christie [c], Mai Sanjoh [d], Weidong Li [c], Shigeto Fukushima [c], Takehiko Ishii [d], Mitsunobu R. Kano [b,e], Nobuhiro Nishiyama [b], Hiroyuki Koyama [a], Kazunori Kataoka [b,c,d,*]

[a] Department of Clinical Vascular Regeneration, Graduate School of Medicine, The University of Tokyo, 7-3-1 Hongo, Bunkyo-ku, Tokyo 113-8655, Japan
[b] Center for Disease Biology and Integrative Medicine, Graduate School of Medicine, The University of Tokyo, 7-3-1 Hongo, Bunkyo-ku, Tokyo 113-0033, Japan
[c] Department of Materials Engineering, Graduate School of Engineering, The University of Tokyo, 7-3-1 Hongo, Bunkyo-ku, Tokyo 113-8656, Japan
[d] Department of Bioengineering, Graduate School of Engineering, The University of Tokyo, 7-3-1 Hongo, Bunkyo-ku, Tokyo 113-8656, Japan
[e] Department of Molecular Pathology, Graduate School of Medicine, The University of Tokyo, 7-3-1 Hong, Bunkyo-ku, Tokyo 113-8655, Japan

ARTICLE INFO

Article history:
Received 11 August 2010
Accepted 24 August 2010
Available online 6 October 2010

Keywords:
Non-viral gene vector
Polyplex micelle
Cholesterol
Pancreatic tumor
Anti-angiogenic therapy

ABSTRACT

Polyplex micelles formed with plasmid DNA (pDNA) and poly(ethylene glycol) (PEG)-*block*-poly{*N*-[*N*-(2-aminoethyl)-2-aminoethyl]aspartamide} [PAsp(DET)] exhibit effective endosomal escaping properties based on di-protonation of diamine side chains with decreasing pH, which improves their transfection efficiency and thus are promising candidates for local *in vivo* gene transfer. Here, PEG-PAsp(DET) polyplex micelles were further improved as *in vivo* systemic vectors by introduction of cholesterol (Chole) into the ω-terminus of PEG-PAsp(DET) to obtain PEG-PAsp(DET)-Chole. Introduction of the cholesterol resulted in enhanced association of block copolymers with pDNA, which led to increased stability in proteinous medium and also in the blood stream after systemic injection compared to PEG-PAsp(DET) micelles. The synergistic effect between enhanced polymer association with pDNA and increased micelle stability of PEG-PAsp(DET)-Chole polyplex micelles led to high *in vitro* gene transfer even at relatively low concentrations, due to efficient cellular uptake and effective endosomal escape of block copolymers and pDNA. Finally, PEG-PAsp(DET)-Chole micelles achieved significant suppression of tumor growth following intravenous injection into mice bearing a subcutaneous pancreatic tumor using therapeutic pDNA encoding an anti-angiogenic protein. These results suggest that PEG-PAsp(DET)-Chole micelles can be effective systemic gene vectors for treatment of solid tumors.

1. Introduction

As expectations for gene therapy increase, so have efforts to develop non-viral vectors with high transfection ability and low toxicity [1,2]. Polyplexes, which are composed of polycations and plasmid DNA (pDNA), are expected as alternatives to viral vectors due to the fine-tuned properties for specific applications by altering the structure of the polycation used for polyplex formation [3–5]. Polyplex micelles formed with poly(ethylene glycol) (PEG)-*block*-polycation block copolymers and pDNA are particularly promising candidates [6–8], due to their excellent characteristics as *in vivo* gene vectors [9,10]. The biocompatible PEG shell layer surrounding the polyplex core contributes to high colloidal stability, allows micelles to maintain their initial size of approximately 100 nm, and reduces non-specific interactions with blood components, which are all desirable properties for systemic administration.

Recently, we reported that polyplex micelles prepared with pDNA and PEG-*block*-poly{*N*-[*N*-(2-aminoethyl)-2-aminoethyl] aspartamide} [PEG-PAsp(DET)] [11] achieved successful *in vitro* transfection of primary cells due to effective endosomal escape of pDNA contained in the micelle core. The PAsp(DET), polycationic segment of the block copolymer is characterized by a distinctive two-step protonation behavior in response to pH and possessed endosomal membrane-selective destabilizing capacity upon acidification [12]. Furthermore, PEG-PAsp(DET) polyplex micelles have shown successful *in vivo* gene transfer by local administration in

* Corresponding author. Department of Materials Engineering, Graduate School of Engineering, The University of Tokyo, 7-3-1 Hongo, Bunkyo-ku, Tokyo 113-8656, Japan. Tel.: +81 3 5841 7138; fax: +81 3 5841 7139.
E-mail address: kataoka@bmw.t.u-tokyo.ac.jp (K. Kataoka).

0142-9612/$ – see front matter © 2010 Elsevier Ltd. All rights reserved.
doi:10.1016/j.biomaterials.2010.09.022

several animal models including: a clamped rabbit carotid artery with neointima without vessel occlusion by thrombus [13], a mouse skull by regulated release from a calcium phosphate cement scaffold to induce bone regeneration through the osteogenic factors [14], and a rat lung pulmonary arterial hypertension model via intratracheal administration [15]. In these cases, however, excess block copolymers relative to pDNA (high N/P ratio) were required to achieve high transfection efficiency, suggesting the existence of free polymer. If free polymer plays a significant role for gene transfer with polyplex micelles prepared from PEG-PAsp (DET) and pDNA, the transfection efficiency under highly diluted conditions, such as systemic application, could be drastically decreased.

The aim of this study was to further develop PEG-PAsp(DET) polyplex micelles towards *in vivo* systemic pDNA delivery vectors. In order to enhance the association of PEG-PAsp(DET) polymers with pDNA and thus increase the efficiency of cellular internalization of polymer necessary for improved endosome escaping, we utilized both electrostatic interaction between polycations and pDNA and hydrophobic interaction by cholesterol to form micelles with improved stability. Specifically, cholesterol was introduced onto the ω-terminus of the PAsp(DET) segment in PEG-PAsp(DET) block copolymer. Cholesterol introduction significantly increased the number of block copolymers associating with a pDNA. *In vitro* experiments were done to demonstrate improved transfection efficiency of PEG-PAsp(DET)-Chole polyplex micelles at low N/P ratios and under the diluted conditions compared to the control micelles formed without cholesterol modified block copolymer. Then, the enhanced stability by the cholesterol introduction in blood was shown, thus allowing successful treatment of a subcutaneous tumor by systemic administration of micelles prepared with PEG-PAsp(DET)-Chole and therapeutic pDNA encoding for an anti-angiogenic protein.

2. Materials and methods

2.1. Materials

Dichloromethane (CH_2Cl_2), *N,N*-dimethylformamide (DMF), triethylamine (TEA), and 3-(4,5-dimethylthiazol-2-yl)-2,5-diphenyltetrazolium bromide (MTT) were purchased from Wako Pure Chem. Co. Ltd. (Osaka, Japan). Cholesterol chloroformate was purchased from Aldrich Chemical Co. Ltd. (Milwaukee, WI). Diethylenetriamine (DET) was purchased from Tokyo Kasei Kogyo (Tokyo, Japan) and distilled over CaH_2 under reduced pressure. DMF was dehydrated using activated molecular sieves (4A) and distilled under reduced pressure. PEG-PAsp(DET) block copolymer (PEG: 12,000 g/mol, polymerization degree of PAsp(DET) segment: 68) was synthesized as previously reported [11]. Alexa Fluor 680 (Alexa680) succinimidyl ester was a product of Invitrogen (Carlsbad, CA). A Micro BCA protein assay reagent kit was purchased from Pierce (Rockford, IL). The Luciferase assay kit was a product of Promega (Madison, WI). Plasmid pCAcc+Luc coding for firefly luciferase under the control of the CAG promoter was provided by RIKEN Gene Bank (Tsukuba, Japan), amplified in competent DH5a *Escherichia coli*, and then purified using a HiSpeed Plasmid MaxiKit purchased from Qiagen Sciences (Germantown, MD). pDNA encoding for a soluble form of VEGF receptor-1 (sFlt-1) was prepared as previously reported [16].

2.2. Animals

Balb/c mice (female, 8 weeks old) and balb/c nude mice (female, 5 weeks old) were purchased from Charles River Laboratories (Tokyo, Japan). All animals were treated in accordance with the guideline of the Animal Ethics Committee of The University of Tokyo.

2.3. Synthesis of α-methoxy-ω-cholesteryl carbamate poly(ethylene glycol)-block-poly{N-[N-(2-aminoethyl)-2-aminoethyl]aspartamide} [PEG-PAsp(DET)]

PEG-*b*-poly(β-benzyl L-aspartate) (PEG-PBLA) (PEG: 12,000 g/mol, polymerization degree of PBLA segment: 68) was prepared as previously reported [11]. PEG-PBLA (210 mg) was dissolved in CH_2Cl_2 (4 mL), followed by the addition of 11 v/v% TEA/CH_2Cl_2 (200 μL) and cholesterol chloroformate (344 mg) in CH_2Cl_2 (1 mL) at 0 °C. The reaction mixture was stirred at room temperature for 24 h. The reactant polymer was isolated by precipitation into diethylether and lyophilized from benzene, to obtain PEG-PBLA-Chole (197 mg). PEG-PBLA-Chole (100 mg) was dissolved in DMF (4 mL), followed by reaction with DET (50 equiv. to benzyl group of PBLA segment, 1.43 g) at 40 °C. After 1 h, the reactant mixture was slowly added to a 20% acetic acid (13.8 mL) solution, and subsequently dialyzed against 0.01 N HCl and finally distilled water. The final solution was lyophilized to obtain PEG-PAsp (DET)-Chole (98 mg).

The ^{1}H NMR spectrum of each polymer was obtained with an EX300 spectrometer (JEOL, Tokyo, Japan). Chemical sifts were reported in ppm relative to the residual protonated solvent peak.

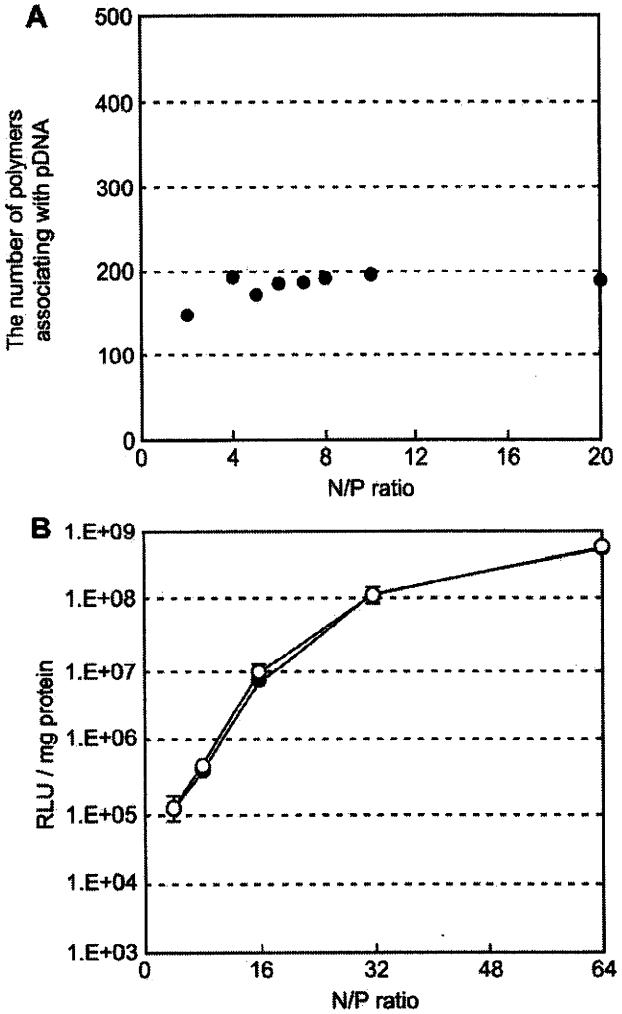

Fig. 1. (A) The number of PEG-PAsp(DET-Alexa680) block copolymers associating with a pDNA. (B) Transfection efficiency of PEG-PAsp(DET) polyplex micelles. Closed circles: addition of polyplex micelle solutions prepared at various N/P ratios into the cell culture medium. Open circles: addition of polyplex micelle solutions prepared at a constant N/P value of 4, with separate addition of PEG-PAsp(DET) free polymer solution into the cell culture medium to obtain the same N/P values shown in the experiment with open circles.

2.4. Introduction of Alexa680 into block copolymers

Alexa680 was introduced into the side chains of both PEG-PAsp(DET) and PEG-PAsp(DET)-Chole polymers. The typical synthetic procedure of PEG-PAsp(DET-Alexa680) is described as follows: Alexa680 succinimidyl ester (1 mg) in 100 μL of DMF was added to PEG-PAsp(DET) (30 mg) in 1.5 mL of 0.1 N $NaHCO_3$ (pH 9.3) and stirred at 4 °C for 1 h. The reacted polymer was purified by dialysis against distilled water and lyophilized to obtain PEG-PAsp(DET-Alexa680) (22 mg). Introduction of Alexa680 into PEG-PAsp(DET)-Chole was completed similarly using Alexa680 succinimidyl ester (1 mg) and PEG-PAsp(DET)-Chole (30 mg) to obtain PEG-PAsp(DET-Alexa680)-Chole (23 mg). The number of Alexa680 introduced into the strand of

PEG-PAsp(DET) and PEG-PAsp(DET)-Chole was estimated to be 0.6 and 0.7, respectively, using a spectrofluorometer (ND-3300, NanoDrop, Wilmington, DE).

2.5. Preparation of polyplex micelles

Each block copolymer and pDNA was dissolved separately in 10 mM Tris–HCl buffer (pH 7.4) or 10 mM Hepes buffer (pH 7.3). Polymer solutions of various concentrations were added to a two-fold excess volume of pDNA solution to form polyplex micelles with different compositions. The final pDNA concentration was adjusted to 33.3 μg/mL for *in vitro* experiments and 100 μg/mL for *in vivo* experiments and micelle solutions were stored at 4 °C overnight prior to use. The N/P ratio was defined as the residual molar ratio of the amino groups of PAsp(DET) units to the phosphate groups of pDNA. The N^+/P ratio was defined as the molar ratio of protonated amino groups of PAsp(DET) units to the phosphate groups of pDNA.

2.6. Ultracentrifugation

In order to evaluate the amount of free polymer in the polyplex micelle solution, ultracentrifugation analysis of polyplex micelles, composed of Alexa680-labeled block copolymers and pDNA, was carried out by a Beckman XL-I ultracentrifuge (Beckman Coulter, Inc., Fullerton, CA) using an An-60 Ti 4-hole rotor and standard double-sectors (Epon centerpieces) equipped with quartz windows. The concentration of polyplex micelle solutions prepared at various N/P ratios were adjusted to 33.3 μg pDNA/mL in 10 mM Hepes buffer (pH 7.3). Sedimentation of polyplex micelles was confirmed by UV absorbance measurement at 260 nm, while that of Alexa680-labeled polymers was confirmed by visible absorbance at 680 nm. Polyplex micelle solutions prepared at various N/P ratios were ultracentrifuged at 49,000 g for 1 h in order to sediment only the polyplex micelles. The concentration of free polymers contained in the supernatant was calculated using a calibration curve prepared from Alexa680-labeled polymer solutions. The number of block copolymers associating with pDNA was then estimated from the calculated concentration of free polymers.

2.7. Dynamic light scattering (DLS) measurement

The size of the polyplex micelles was evaluated by DLS using Nano ZS (ZEN3600, Malvern Instruments, Ltd., UK). A He–Ne ion laser (633 nm) was used as the incident beam. The concentration of polyplex micelle solutions prepared at various N/P ratios were adjusted to 33.3 μg pDNA/mL in 10 mM Tris–HCl buffer (pH 7.4). Light scattering data was obtained at a detection angle of 173° and a temperature of 37 °C and was subsequently analyzed by the cumulant method to obtain the hydrodynamic diameters and polydispersity indices (PDI) (μ/I^2) of the micelles.

2.8. Stability of polyplex micelles against bovine serum albumin (BSA)

Polyplex micelle solution (33.3 μg pDNA/mL) prepared at N/P ratio = 2 was adjusted to 10 μg pDNA/mL in 10 mM Tris–HCl buffer (pH 7.4) with 150 mM NaCl and 0.1 mg/mL BSA. DLS measurements of the polyplex micelle solution were then carried out every 30 min at 37 °C using Nano ZS.

2.9. In vitro transfection

Huh-7 and HeLa cells were separately seeded onto 24-well culture plates (10,000 cells/well) and incubated overnight in 500 μL of Dulbecco's Modified Eagle Medium (DMEM) containing 10% fetal bovine serum (FBS). The medium was exchanged and the pDNA micelle solutions (33.3 μg pDNA/mL) prepared at various N/P ratios were applied to each well at the desired concentrations. The amount of micelle solution added was as follows: 30 μL for 2 μg pDNA/mL, 10 μL for 2/3 μg pDNA/mL, or 3.3 μL for 2/9 μg pDNA/mL. For experiments shown in Fig. 1B (open circles), polymer solution was added to cultured Huh-7 cells simultaneously with PEG-PAsp(DET) micelle (N/P = 4), in order to elucidate the effect of free polymer on transfection efficiency. After 24-h incubation, the medium was replaced with 500 μL of fresh medium, followed by 24-h further incubation. Luciferase gene expression was then evaluated based on photoluminescence intensity using the Luciferase assay kit and a Luminometer (Lumat LB9507, Berthold Technologies, Bad Wildbad, Germany). The amount of protein in each well was concomitantly determined using a Micro BCA protein assay kit. One nanogram of luciferase corresponded to 9.1×10^7 RLU in our experiments according to a standard curve calibrated with recombinant luciferase (QuantiLum, Promega).

2.10. Cytotoxicity of polyplex micelles

Huh-7 and HeLa cells were separately seeded onto 96-well culture plates (2500 cells/well) and incubated overnight in 100 μL of DMEM containing 10% FBS. After the medium was replaced with fresh medium, 7.5 μL of polyplex micelle solution (33.3 μg pDNA/mL) prepared at various N/P ratios was applied to each well (0.25 μg pDNA/well). After 24-h incubation, the medium was replaced with 100 μL of fresh medium, followed by 24-h incubation. Cell viability was evaluated using the MTT assay. Briefly, 20 μL of MTT solution (5 mg/mL in PBS) was added to each well, followed by 3-h incubation at 37 °C. Then, 100 μL of sodium dodecyl sulfate (SDS) solution (20 w/v% in PBS) was added to dissolve the formed formazan. After 15-min incubation at room temperature, the absorbance from each well was measured at 570 nm. Results were expressed as percentage relative to non-treated controls.

2.11. Cellular uptake of polymers and pDNA

Polyplex micelles were prepared with non-labeled polymer and Cy3-labeled pDNA (Fig. 8A), or with Alexa680-labeled polymer and non-labeled pDNA (Fig. 8B) for these experiments. pDNA was labeled with Cy3 using a Label IT Nucleic Acid Labeling Kit (Mirus, Madison, WI) according to the manufacturer's protocol. Huh-7 cells were seeded on 24-well culture plates (10,000 cells/well) and incubated overnight in 500 μL of DMEM containing 10% FBS. The medium was replaced with fresh medium and then 30 μL of polyplex micelle solution (33.3 μg pDNA/mL) was applied to each well. After 24-h incubation, the medium was removed and the cells were washed 3 times with PBS and detached with trypsin. Harvested cells were re-suspended in PBS and analyzed using the flow cytometer (BD LSR II, BD, Franklin Lakes, NJ).

2.12. Confocal laser scanning microscope (CLSM) observation

pDNA was labeled with Cy5 according to manufacturer's protocol using a Label IT Nucleic Acid Labeling Kit. Huh-7 cells (30,000) were seeded on a 35-mm glass base dish (Iwaki, Tokyo, Japan) and incubated overnight in 1.5 mL of DMEM containing 10% FBS. After the medium was exchanged, 90 μL of polyplex micelle solution (33.3 μg pDNA/mL) was applied to each sample. After 24-h incubation, the medium was removed and the cells were washed three times with PBS. The intracellular distribution of the polyplex micelles was observed by CLSM after staining acidic late endosomes/lysosomes with LysoTracker Green (Molecular Probes, Eugene, OR), and nuclei with Hoechst 33342 (Dojindo Laboratories, Kumamoto, Japan). CLSM observation was performed using an LSM 510 (Carl Zeiss, Oberlochen, Germany) equipped with a 63× objective (C-Apochromat, Carl Zeiss) at the excitation wavelengths of 488 nm (Ar laser) for Lyso Tracker Green, 633 nm (He–Ne laser) for Cy5, and 710 nm (MaiTai laser, 2 photon excitation; Spectra-Physics, Mountain View, CA) for Hoechst 33342. To evaluate the endosomal escaping behavior of polyplex micelles, the rate of colocalization of Cy5-labeled pDNA with Lyso Tracker Green was quantified [17]. Colocalization was quantified as follows:

$$\text{Amount of colocalization}(\%) = \text{Cy5 pixels}_{\text{colocalization}}/\text{Cy5 pixels}_{\text{total}} \times 100$$

where $\text{Cy5 pixels}_{\text{colocalization}}$ represents the number of Cy5 pixels colocalizing with Lyso Tracker Green in the cell, and $\text{Cy5 pixels}_{\text{total}}$ represents the number of all the Cy5 pixels in the cell.

2.13. Fluorescence correlation spectroscopy (FCS) measurement

PEG-PAsp(DET-Alexa680)-Chole free polymer, polyplex micelles composed of PEG-PAsp(DET-Alexa680)-Chole and pDNA, and polyplex micelles composed of PEG-PAsp(DET) and Cy5-labeled pDNA, were used in this experiment. Block copolymers and polyplex micelles (N/P = 8) were adjusted to a polymer concentration of 187 μg/mL (33.3 μg pDNA/mL) in 10 mM Hepes buffer (pH 7.3), and then diluted to a concentration of 18.7 μg/mL using 10 mM Hepes buffer (pH 7.3) (Fig. 10A) or 10 mM MES buffer (pH 5.5) (Fig. 10B), or 2.08 μg/mL using 10 mM Hepes buffer (pH 7.3) (Fig. 10A). FCS measurements were carried out using an LSM 510 (Carl Zeiss) equipped with a 40× objective (C-Apochromat, Carl Zeiss) and the ConfoCor3 module. Excitation of Alexa680 and Cy5 was achieved with a He–Ne laser (633 nm). The relative diffusion times of polymer and micelles (Fig. 10A) were determined using PEG-PAsp(DET-Alexa680)-Chole solution and its polyplex micelle solution, respectively. Furthermore, the percentage of polymers associating with pDNA in the micelle solution was calculated as follows:

$$\text{Percentage.of polymers associating with pDNA} = \left[\text{Nfp}_{\text{PEG-PAsp(DET-Alexa680)-Chole}} - \left(\text{Nfp}_{\text{PEG-PAsp(DET-Alexa680)-Chole/pDNA}} - \text{Nfp}_{\text{PEG-Pasp(DET)-Chole/Cy5-pDNA}}\right)\right] / \text{Nfp}_{\text{PEG-PAsp(DET-Alexa680)-Chole}} \times 100$$

where $\text{Nfp}_{\text{PEG-PAsp(DET-Alexa680)-Chole}}$ represents the number of fluorescent particles (free polymers) in PEG-PAsp(DET-Alexa680)-Chole solution, $\text{Nfp}_{\text{PEG-PAsp(DET-Alexa680)-Chole/pDNA}}$ represents the number of fluorescent species (free polymers and micelles) in PEG-PAsp(DET-Alexa680)/pDNA micelle solution, and $\text{Nfp}_{\text{PEG-Pasp(DET)-Chole/Cy5-pDNA}}$ represents the number of fluorescent species (micelles) in PEG-PAsp (DET)-Chole/Cy5-pDNA micelle solution.

2.14. Stability of polyplex micelles in the blood stream

Polyplex micelles (N/P = 8) incorporating Cy5-labeled pDNA (100 μg pDNA/mL, 200 μL) in 10 mM Hepes buffer (pH 7.3) with 150 mM NaCl were intravenously injected into the tail vein of balb/c mice at a dose of 20 μg pDNA/mouse. Blood

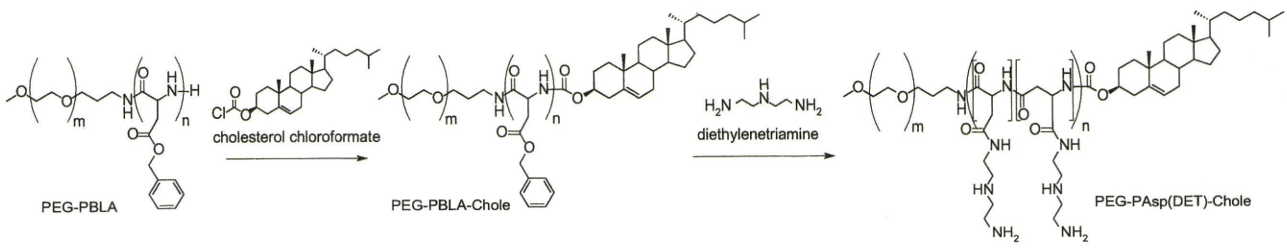

Scheme 1. Synthesis of PEG-PAsp(DET)-Chole block copolymer.

was collected from the postcaval vein under anesthesia at appointed times after injection, followed by centrifugation to obtain the plasma. Two microliters of 10× trypsin-EDTA were added to 20 μL of the obtained plasma and incubated at 37 °C overnight. The fluorescence intensity of the sample solution was measured using a spectrofluorometer (ND-3300, NanoDrop). The injected dose (%) was calculated using a standard curve.

2.15. Anti-tumor activity assay

Balb/c nude mice were inoculated subcutaneously with human pancreatic adenocarcinoma BxPC3 cells (5×10^6 cells in 100 μL of PBS). Tumors were allowed to grow for 2–3 weeks to reach proliferative phase (approximately 45 mm^3). Subsequently, polyplex micelles loading pDNA encoding sFlt-1 (20 μg pDNA/mouse) in 10 mM Hepes buffer (pH 7.3) with 150 mM NaCl were injected into the tail vein 3 times at 4-day intervals. Tumor volume (V) was calculated as the following equation:

$$V = a \times b^2/2$$

where a and b denote the long and short diameters of the tumor tissue, respectively.

3. Results

3.1. Ultracentrifugation analysis of PEG-PAsp(DET) polyplex micelles

The amount of free block copolymer in PEG-PAsp(DET) micelle solutions was quantified by ultracentrifugation analysis of polyplex micelles prepared with fluorescent-labeled block copolymer [PEG-PAsp(DET-Alexa680)]. Polyplex micelles were confirmed to precipitate after 1 h of ultracentrifugation at 49,000 g, whereas free block copolymers could not sediment (data not shown). Thus, the amount of free block copolymers was estimated by visible absorbance at 680 nm. Fig. 1A shows the number of block copolymers associating with a pDNA in the polyplex micelle solution prepared at each N/P ratio. Note that a stoichiometric charge ratio of PEG-

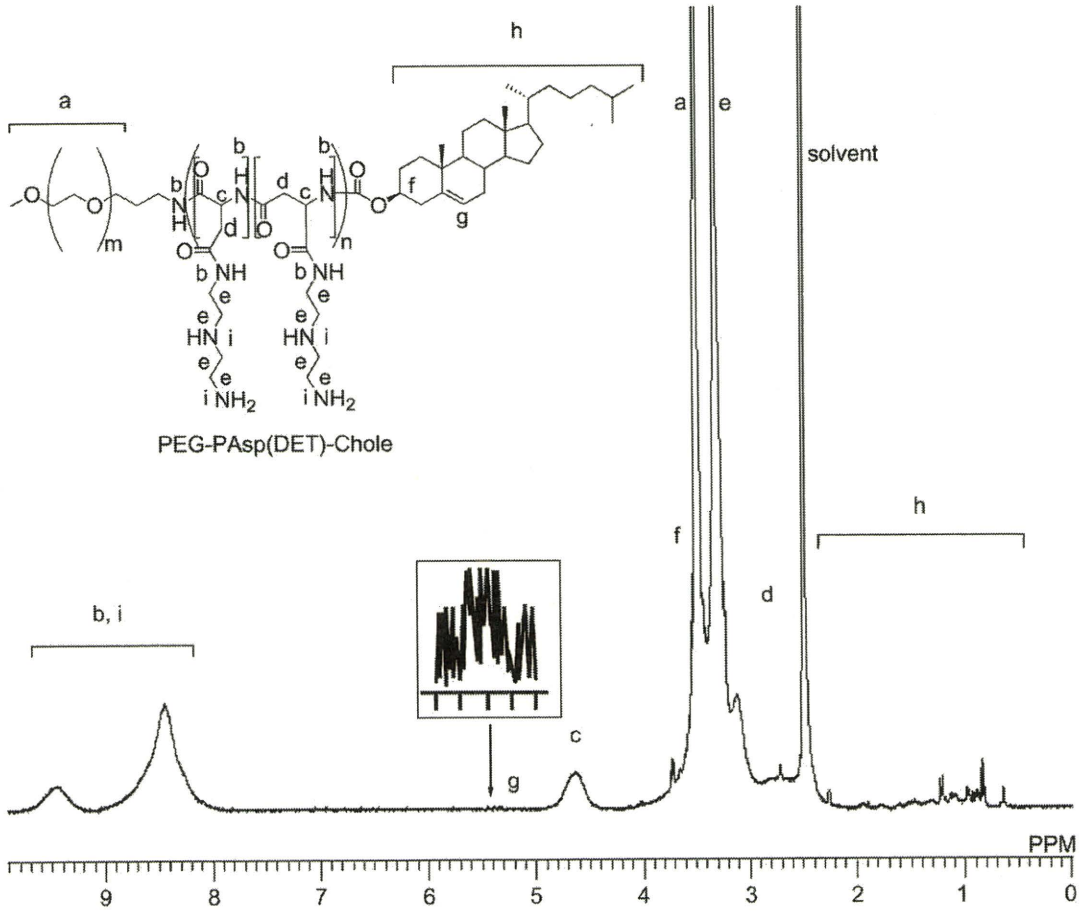

Fig. 2. ^{1}H NMR spectrum of PEG-PAsp(DET)-Chole block copolymer in DMSO at 25 °C.